J. Fluid Mech. (2023), *vol*. 964, A8, doi:10.1017/jfm.2023.329

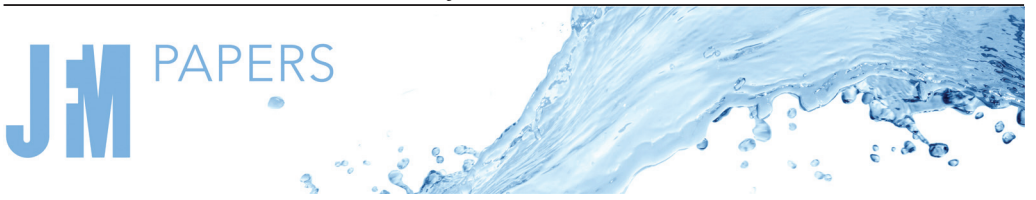

Reynolds number dependence of the turbulent/non-turbulent interface in temporally developing turbulent boundary layers

Xinxian Zhang[1,2,†], **Tomoaki Watanabe**[3] **and Koji Nagata**[4]

[1]School of Aeronautic Science and Engineering, Beihang University, Beijing 100191, PR China

[2]Department of Aerospace Engineering, Nagoya University, Nagoya 464-8603, Japan

[3]Education and Research Center for Flight Engineering, Nagoya University, Nagoya 464-8603, Japan

[4]Department of Mechanical Engineering and Science, Kyoto University, Kyoto 615-8540, Japan

(Received 2 August 2022; revised 25 January 2023; accepted 8 April 2023)

Direct numerical simulations (DNS) of temporally developing turbulent boundary layers are performed with a wide range of Reynolds numbers based on the momentum thickness $Re_\theta = 2000$–$13\,000$ for investigating the Reynolds number dependence of the turbulent/non-turbulent interface (TNTI) layer. The grid spacing in the DNS is determined carefully such that small-scale turbulent motions near the TNTI are well resolved. The outer edge of the TNTI layer, called the irrotational boundary, is detected with vorticity magnitude. The mean thicknesses of the TNTI layer, δ_{TNTI}, turbulent sublayer, δ_{TSL}, and viscous superlayer, δ_{VSL}, are found to be approximately $15\eta_{TI}$, $10\eta_{TI}$ and $5\eta_{TI}$, respectively, where η_{TI} is the Kolmogorov scale taken in the turbulent region near the TNTI layer. The mean curvature of the irrotational boundary is also characterized by η_{TI}. The shear parameter and the shear-to-vorticity ratio show that the mean shear effects near the TNTI layer are not significant for both large and small scales. The anisotropy tensors of Reynolds stress and vorticity suggest that the turbulence under the TNTI layer tends to be isotropic at high Re_θ, for which $\eta_{TI}/\delta \sim Re_\theta^{-3/4}$ is valid with the boundary layer thickness δ. The surface area of the irrotational boundary is consistent with the fractal analysis of the interface, where the fractal dimension D_f is found to be 2.14–2.20. The present results suggest that the mean entrainment rate per unit horizontal area normalized by the friction velocity varies slowly as $Re_\theta^{(3/4)(D_f-2)}$ for $Re_\theta \geq 4000$.

Key words: turbulent boundary layers, turbulence simulation, intermittency

† Email address for correspondence: zhangxinxian@buaa.edu.cn

1. Introduction

A turbulent boundary layer (TBL) plays a significant role in many engineering applications and atmospheric science. For example, a flow passing through a vehicle can affect the efficiency of the vehicle; the atmospheric TBL is very important for weather prediction. Many recent works show that there exists a thin layer with a finite thickness that separates the turbulent and non-turbulent flows in many turbulent flows, e.g. jet, mixing layer and boundary layer (da Silva *et al.* 2014). This thin layer is called the turbulent/non-turbulent interface (TNTI), whose existence was pointed out by Prandtl (1928) and examined by Corrsin & Kistler (1955).

With the improvement of experimental technologies and computational resources in recent years, the TNTI layer has been investigated in free shear flows (da Silva & Pereira 2008; Westerweel *et al.* 2009; Watanabe *et al.* 2015) and TBLs (de Silva *et al.* 2013, 2017; Chauhan *et al.* 2014*b*; Philip *et al.* 2014; Ishihara, Ogasawara & Hunt 2015; Borrell & Jiménez 2016; Lee, Sung & Zaki 2017; Zhang, Watanabe & Nagata 2018; Jahanbakhshi 2021). The TNTI layer consists of two sublayers: the outer part bounded to the irrotational flow is called the viscous superlayer (VSL), where viscous effects dominate the increase of vorticity magnitude; the turbulent sublayer (TSL), where the inviscid effects become important, exists as a buffer layer between the VSL and the turbulent core region (da Silva *et al.* 2014). Since the TNTI layer separates the turbulent and non-turbulent flow regions, the flow properties in these two regions are highly different. This layer is significant for the exchanges of substance, energy and heat between turbulent and non-turbulent flow, and is related to the development of turbulence (Holzner & Lüthi 2011). The Reynolds number dependence is one of the most important issues in the study of the TNTI layer; it represents the essential properties of the TNTI layer, and contributes to the understanding of flow behaviour near here, and is related to the scaling of the entrainment, which causes the development of the turbulent region (van Reeuwijk, Vassilicos & Craske 2021). That can also consequently provide useful information for the modelling and flow control of turbulence as the entrainment is considered caused by the vorticity structures within the TNTI layer (Watanabe *et al.* 2017*a*; Neamtu-Halic *et al.* 2020).

In previous literature, the scaling of the mean thickness of the TNTI layer δ_{TNTI} has been argued about extensively. This mean thickness was first measured by Bisset, Hunt & Rogers (2002) in turbulent wakes and shown to be approximately one order of the Taylor microscale λ. Other studies also suggested that δ_{TNTI} is of the same order as the Taylor microscale λ in the mixing layer (Attili, Cristancho & Bisetti 2014), jet (Westerweel *et al.* 2009) and boundary layer (Chauhan, Philip & Marusic 2014*a*; Borrell & Jiménez 2016). In contrast, other studies showed that δ_{TNTI} is scaled by the Kolmogorov scale $\eta = \nu^{3/4}\langle\varepsilon\rangle^{-1/4}$ in the jet (Nagata, Watanabe & Nagata 2018; Silva, Zecchetto & da Silva 2018), shear-free turbulence (Holzner *et al.* 2007; Silva *et al.* 2018) and mixing layer (Watanabe *et al.* 2015), where $\langle\varepsilon\rangle$ is the turbulent kinetic energy dissipation rate, and ν is the kinematic viscosity. Also, Jahanbakhshi (2021) suggested that the VSL is scaled by η in the TBL. Silva *et al.* (2018) summarized most of the recent studies and investigated systematically the scaling of δ_{TNTI} in the planar jet and shear-free turbulence. They showed that δ_{TNTI}/λ decreases as the Reynolds number increases, while δ_{TNTI}/η is independent of the Reynolds number except for very low Reynolds numbers. However, the scaling of δ_{TNTI} is still an open question, especially in the TBL, where the TNTI layer is less studied compared with free shear flows.

Other turbulent statistics near and within the TNTI layer in the TBL also need to be investigated, e.g. turbulent kinetic energy, vorticity and strain distribution, and shear

effects. How these statistics vary with the Reynolds number is also an important issue. In particular, the mean shear effect is an important issue for scaling the mean thickness of the TNTI layer. Hunt *et al.* (2010) used the Burgers vortex model to explain the scaling of δ_{TNTI}, which is expected to be $\delta_{TNTI} \sim \lambda$ under the strong influence of mean shear, and $\delta_{TNTI} \sim \eta$ without shear. Even though Watanabe *et al.* (2017*c*) showed that the mean thickness of the TNTI layer is the same in turbulent planar jets and shear-free turbulence, the mean shear effect still needs to be investigated more carefully in TBLs because the degree of mean shear effects can be flow-dependent.

The geometry of the TNTI is also important because it is related the entrainment rate, which depends on the surface area of the TNTI (Holzner & Lüthi 2011). The geometry of the TNTI is dependent on the turbulent structures under the TNTI, which can be flow-dependent and may affect the universality of the geometry of the TNTI layer. The TNTI has a complex shape and exhibits fractal-like properties, as shown in the previous studies (da Silva *et al.* 2014). But it is still unclear if the interface geometry has universal statistical properties that do not depend on flows and Reynolds numbers (da Silva *et al.* 2014). The entrainment is understood as a process by which an irrotational fluid becomes a part of the turbulent flow while it passes across the TNTI layer. The irrotational fluid becomes turbulent near the TNTI layer by the viscous diffusion of vorticity (Holzner & Lüthi 2011; Mistry *et al.* 2016), which is called local entrainment. Therefore, the viscous effects are important for the local entrainment rate, which represents the volume of entrained fluid per unit interface area and per time. In recent studies (da Silva *et al.* 2014), the nibbling process (local entrainment) is also shown to be the main contributor to the entrainment process in the TBL, and the intense vortex structures (worms) close to the TNTI are dominant in the nearby entrainment velocity. In addition, the total entrainment rate can be evaluated as an integral of the local entrainment velocity over the interface. The total entrainment rate depends strongly on the surface area of the interface, which is also influenced by large-scale motions of the flow. Even some existing studies (Watanabe *et al.* 2015; Nagata *et al.* 2018) show that the entrainment velocity v_n is the order of the Kolmogorov velocity scale v_η in shear-free flows. However, the entrainment is a multiscale process, which means that the large-scale motions are also involved (Mistry *et al.* 2016). Some recent studies showed that the large-scale motions do modulate the entrainment velocity in the TBL (Long, Wang & Pan 2022) and jet (Cimarelli & Boga 2021). Furthermore, the large-scale motions are shown to dominate the mass and energy transport in the outer region (Adrian, Meinhart & Tomkins 2000) in TBL.

There are several previous studies on the Reynolds number dependence of the TNTI layer in the TBL: Chauhan *et al.* (2014*a*) used the experimental data ($Re_\tau = u_\tau \delta_\nu / \nu =$ 1230–14 500) to study the Reynolds number dependence of the TNTI layer in the TBL. However, the TNTI layer in this study is detected with velocity, where the TNTI layer is treated as a shear layer. Since the seminal work on the TNTI by Corrsin & Kistler (1955), it has been known that the TNTI is not well-defined in the profiles of velocity or kinetic energy. As Corrsin & Kistler (1955) pointed out, rotational motion is the essential feature of the turbulent flow region, and the TNTI is well-defined only with the quantities related to vorticity. Therefore, Corrsin & Kistler (1955) had to apply a complicated post-process on velocity signals obtained with hot-wire anemometry to detect turbulent regions because the velocity or kinetic energy could not distinguish the turbulent and non-turbulent regions well. They define the detector function of the TNTI with a time derivative of velocity, which is related to a velocity gradient. Therefore, their detection method of the TNTI is closer to the vorticity criterion than the kinetic energy criterion.

The interfaces defined with enstrophy and kinetic energy were compared in temporally evolving TBLs in Watanabe, Zhang & Nagata (2018*b*). It was found that the interfaces detected with these quantities are very different in terms of both geometry and location. Small-scale structures are missing on some parts of the interface detected with kinetic energy (Watanabe *et al.* 2018*b*). The conditional statistics calculated for the interfaces of enstrophy and kinetic energy were also different, except for low-order statistics of velocity, such as mean velocity and velocity variance. This may be because the pressure diffusion at large scales transfers the kinetic energy from the turbulent to the non-turbulent region, while the pressure term does not appear in the enstrophy transport equation. Borrell & Jiménez (2016) have studied the TNTI detected with vorticity using the direct numerical simulations (DNS) database of the TBL. However, the Reynolds number range is still limited for $Re_\theta = U_W\theta/\nu = 2800$–$6800$ ($Re_\tau = 1000$–2000) based on the momentum thickness $\theta = \int_0^\infty \langle u\rangle(U_W - \langle u\rangle)/U_W^2\,\mathrm{d}y$. These values of Re_θ are in the transitional range of low to moderate Reynolds number, and the scale range of turbulent motions is still small, so some typical phenomena in TBL are not obvious yet. The higher Reynolds number is necessary for examining the Reynolds number dependence.

The Reynolds number dependence of the TNTI layer is a significant topic in TNTI studies. However, this investigation still lacks information, especially for the TBL. If DNS are used for studying the TNTI layer in the TBL, then the resolution near the TNTI layer needs to be considered carefully because the smallest length scale of turbulence is different between the outer and near-wall regions, where the resolution determined based on the near-wall region can be insufficient for studying the TNTI layer (Watanabe *et al.* 2018*b*; Zhang *et al.* 2018). In addition, the wall can have a strong influence on the TNTI layer in the TBL (Lee *et al.* 2017), but this influence has not been studied well in previous papers.

In this study, we conduct DNS of temporally developing incompressible TBLs for a wide range of Reynolds numbers $Re_\theta = 2000$–$13\,000$ ($Re_\tau = 700$–4000). The spatial resolution of the DNS is determined carefully such that the smallest scale of turbulent motions is well resolved near the TNTI layer. The detail of the DNS database is presented in § 2. Section 3 discusses the Reynolds number dependence of the TNTI layer as well as the mean shear effects on the TNTI layer, the geometrical properties of the TNTI layer, and the entrainment process. Finally, § 4 presents the conclusion of this study.

2. The DNS of temporally developing turbulent boundary layers

2.1. *Temporally developing turbulent boundary layers*

A DNS database of incompressible temporally developing TBLs (Watanabe, Zhang & Nagata 2019*b*) is used in this study. A temporally evolving TBL is proposed by assuming that the boundary layer grows so slowly in the streamwise direction that the turbulence can be treated as approximately homogeneous in this direction (Spalart 1988). This idea has been adapted to various canonical turbulent shear flows, e.g. TBLs (Martín 2007; Guarini *et al.* 2000; Kozul, Chung & Monty 2016), mixing layers (Vreman, Sandham & Luo 1996; Watanabe *et al.* 2015) and jets (Hawkes *et al.* 2007; Nagata *et al.* 2018; Silva *et al.* 2018). These studies have proved that the transverse profile of most statistics is consistent between spatially and temporally evolving flows. The temporally evolving TBL may be called a turbulent Rayleigh shear flow, which is equivalent to a spatially evolving TBL at infinite Reynolds number (Crow 1968). Although the temporal and spatial TBLs are different in a strict sense at a finite Reynolds number, the vertical profiles of most statistics become asymptotically equivalent in these flows at a sufficiently large Reynolds number ($Re_\theta \gtrapprox$

2000) when the Reynolds number based on the diameter of a trip wire D, applied in the initial condition, is $Re_D = 2000$ (Kozul *et al.* 2016; Zhang *et al.* 2018). These studies also suggest that the mean shear effect caused by the transverse inhomogeneity is well captured by numerical simulations of temporally evolving TBLs.

The purpose of this study is to investigate the TNTI in wall-bounded shear flows for a wide range of Reynolds numbers, which is discussed by comparison with previous studies on the TNTI in turbulent free shear flows. The computational cost is much lower for temporally evolving flows than spatially evolving ones for the same Reynolds number. Therefore, the temporal TBL is an appropriate choice because a higher Reynolds number can be achieved by temporal simulations for a given computational resource. The governing equations are the three-dimensional incompressible Navier–Stokes equations, which can be expressed as

$$\frac{\partial u_j}{\partial x_j} = 0, \tag{2.1}$$

$$\frac{\partial u_i}{\partial t} + \frac{\partial u_i u_j}{\partial x_j} = -\frac{1}{\rho}\frac{\partial p}{\partial x_i} + \nu \frac{\partial^2 u_i}{\partial x_j \partial x_j}. \tag{2.2}$$

Here, u_i is the instantaneous velocity in the i direction; the subscripts $i, j = 1, 2, 3$ indicate the x, y and z directions, respectively; ρ is the constant fluid density; and p is the instantaneous pressure. The velocity components in the x, y and z directions are denoted by u, v and w, respectively. We consider the TBL developing on a wall moving at a constant speed U_W, where the subscript W refers to a value on the wall. The temporal simulation uses periodic boundary conditions in the streamwise (x) and spanwise (z) directions, and the statistics do not vary in the streamwise direction. The wall-normal direction is denoted by y. A no-slip condition is used on the wall ($y = 0$), and a slip condition is applied at the top of the computational domain. Spatial averages denoted by $\langle\cdot\rangle$ taken on an x–z plane are obtained as functions of y and time. Hereafter, the fluctuation from this average is denoted as $f' = f - \langle f\rangle$.

The initial mean streamwise velocity profile approximates the velocity induced by a trip wire with diameter D installed on the wall (Kozul *et al.* 2016):

$$\langle u\rangle = \frac{U_W}{2} + \frac{U_W}{2}\tanh\left[\frac{D}{2\theta_{sl}}\left(1 - \frac{y}{D}\right)\right], \tag{2.3}$$

with the initial shear layer thickness $\theta_{sl} = 0.03D$, while the mean velocity in other directions is 0. Velocity fluctuations with root mean square (r.m.s.) value $0.05U_W$ are also added in the near-wall region of $y \le D$. In this study, the flow is characterized by the Reynolds number based on the trip wire diameter $Re_D = U_W D/\nu = 2000$, which is large enough for turbulent transition to occur (Kozul *et al.* 2016).

2.2. *Computational parameters*

The DNS are performed with six different Reynolds numbers, as summarized in table 1, which also shows the size of the computational domain (L_x, L_y, L_z) and the number of grid points (N_x, N_y, N_z). In each simulation, time is advanced until Re_θ reaches the value shown in the table. Table 2 summarizes the Reynolds numbers $Re_\delta = U_W\delta/\nu$ and $Re_\tau = u_\tau\delta_\nu/\nu$, the computational domain size divided by δ, and the grid size normalized by the viscous length scale δ_ν or the Kolmogorov scale η at the end of the DNS. Here, $u_\tau = \sqrt{\tau_W/\rho}$ is the friction velocity, $\tau_W = -\rho\nu(\partial\langle u\rangle/\partial y)_W$ is the wall shear stress, and the viscous

Case	Re_θ	L_x/D	L_y/D	L_z/D	N_x	N_y	N_z
B02	2000	56	76	28	1024	648	512
B04	4000	120	162	60	1536	864	1024
B06	6000	170	230	85	2048	1152	1536
B08	8000	220	298	110	2916	1728	1458
B10	10 000	276	360	138	3456	2048	2592
B13	13 000	360	480	180	4608	2700	3456

Table 1. Computational parameters of the DNS of a temporally developing TBL.

Case	Re_θ	Re_τ	Re_δ	L_x/δ	L_y/δ	L_z/δ	Δ_x^+	Δ_y^+	Δ_z^+	Δ_x/η	Δ_y/η	Δ_z/η
B02	2000	706	16 517	6.7	9.1	3.4	4.7	0.13	4.7	1.4	1.2	1.4
B04	4000	1312	33 774	7.1	9.6	3.6	6.1	0.19	4.1	1.5	1.3	1.1
B06	6000	1845	49 567	6.9	9.3	3.4	6.2	0.19	4.1	1.4	1.3	0.9
B08	8000	2538	71 175	6.2	8.4	3.1	5.5	0.16	5.5	1.2	1.1	1.2
B10	10 000	3058	85 528	6.5	8.4	3.2	5.7	0.16	3.8	1.2	1.1	0.8
B13	13 000	3980	113 182	6.4	8.5	3.2	5.5	0.16	3.7	1.1	1.0	0.7

Table 2. Reynolds numbers, computational domain size divided by δ, and grid size normalized by the viscous length scale δ_v or Kolmogorov scale η at the end of the DNS. Here, Δ_y^+ and Δ_i/η are taken on the wall and at $y/\delta = 0.5$, respectively.

length scale is defined as $\delta_v = \nu/u_\tau$. The superscript $+$ denotes a quantity normalized by the wall unit. The Kolmogorov scale η and Δ_y are taken at $y/\delta = 0.35$ (where δ is 99 % boundary layer thickness based on the mean velocity profile). The computational domain (L_x, L_y, L_z) in table 1 is determined such that the conditions $L_x \geq 2\pi\delta$, $L_y > \delta$ and $L_z \geq \pi\delta$ are satisfied as in previous studies (Schlatter & Örlü 2010; Lozano-Durán & Jiménez 2014; Kozul *et al.* 2016). The number of the grid points is determined based on the grid size Δ_i compared with the length scale both near the wall δ_v and in turbulence η $(y/\delta = 0.5)$. The uniform grid spacing is applied in the x and z directions, while the vertical location of the grid points is determined by the mapping function as employed in Zhang *et al.* (2018) and Watanabe *et al.* (2018*b*), where the grid size becomes smaller near the wall. The present DNS satisfy $\Delta_i \leq 1.5\eta$ at $y/\delta = 0.5$ because the present study investigates the TNTI layer that appears in the outer region. So Δ_i^+ is smaller than the grid size widely used in DNS of wall turbulence ($\Delta_x^+ < 9.7$, $\Delta_y^+ < 0.2$ and $\Delta_z^+ < 4.8$; Moser, Kim & Mansour 1999), especially for the x direction. The grid size in the present DNS is small enough to study the TNTI layer in the TBL, and further discussion on the effects of spatial resolution on the TNTI in the TBL can be found in our previous studies (Watanabe *et al.* 2018*b*; Zhang *et al.* 2018).

The present DNS are initialized with an implicit large eddy simulation (ILES); the computational parameters of ILES used for initialization and the numerical methods are shown in Appendix A. Furthermore, Appendix B examines the effects of the computational domain size, and shows that the main results presented in this paper are not influenced by the finite domain size used in the present study.

2.3. *Comparisons of statistics with experiment and spatial DNS studies*

The present DNS results are validated by comparing the statistics with experiments at similar Re_θ and theoretical laws. Figure 1 shows the mean streamwise velocity $U^+ =$

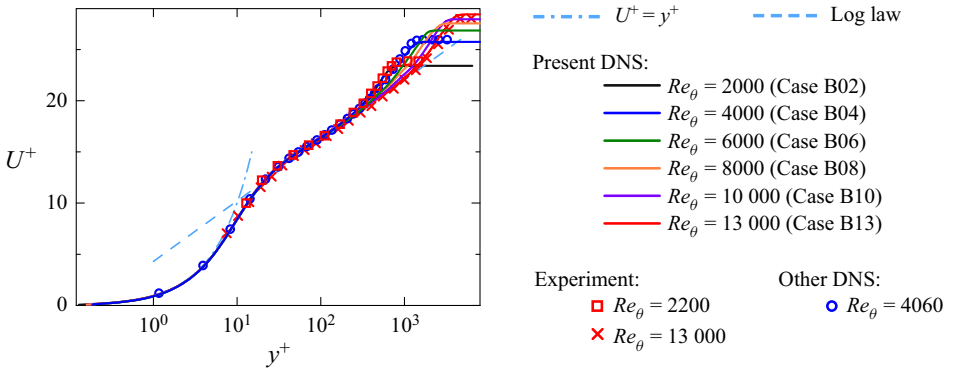

Figure 1. The mean profiles of streamwise velocity U^+ compared with experimental results with $Re_\theta = 2200$ ($Re_\tau = 810$; Erm & Joubert 1991) and $Re_\theta = 13\,000$ ($Re_\tau = 4336$; De Graaff & Eaton 2000), and previous spatial DNS results $Re_\theta = 4060$ ($Re_\tau = 1271$; Schlatter & Örlü 2012). The dashed line represents the log law $U^+ = (1/k)\ln y^+ + A$ (Pope 2000) with the constants $k = 0.39$ and $A = 4.3$ (Marusic *et al.* 2013).

$\langle u \rangle / u_\tau$, which is compared with the experimental data for $Re_\theta = 2200$ (Erm & Joubert 1991), $Re_\theta = 13\,000$ (De Graaff & Eaton 2000), and previous spatial DNS data for $Re_\theta = 4060$ (Schlatter & Örlü 2012). Here, all quantities in the plots are normalized with the viscous scales. Present DNS results follow $U^+ = y^+$ for small y^+ ($y^+ \lesssim 5$), and the results start to follow the log law for larger y^+. We can also see that U^+ in the experiments is similar to the present DNS data at $Re_\theta = 2000$ and $Re_\theta = 13\,000$. Figure 2 shows the r.m.s. of streamwise and vertical velocity fluctuations ($u_{rms} = \sqrt{\langle u'^2 \rangle}$ and $v_{rms} = \sqrt{\langle v'^2 \rangle}$) and Reynolds stress $\langle u'v' \rangle$ at the end of the DNS in comparison with experimental studies (Osaka *et al.* 1998; De Graaff & Eaton 2000; Carlier & Stanislas 2005) and previous spatial DNS studies (Schlatter & Örlü 2012; Sillero *et al.* 2013). It should be noticed that only $Re_\theta = 2000$–6000 are compared with the previous DNS due to the lack of DNS data for the higher Reynolds number range. For all Reynolds numbers, the DNS results agree well with experimental data and spatial DNS data with a comparable value of Re_θ, and the present DNS well capture the Reynolds number dependence of the TBL. Reynolds number dependence of other quantities, e.g. skin friction, spectral shape, and skewness and flatness of velocity derivative, was further compared with experiments and DNS in Watanabe *et al.* (2019*b*), where the present DNS results were shown to agree well with previous studies of the TBL.

3. Results and discussions

3.1. *Detection of the TNTI layer*

Following previous studies (da Silva *et al.* 2014), an isosurface of vorticity magnitude $\omega = \omega_{th}$ is used to detect the outer edge of the TNTI layer, which is called the irrotational boundary (Watanabe *et al.* 2015). Obviously, the location of the isosurface changes with the threshold value ω_{th}. In this method, a fluid point with $\omega > \omega_{th}$ is denoted as a turbulent fluid point, while a non-turbulent fluid point has $\omega < \omega_{th}$. For determining an appropriate value of ω_{th} for studying the TNTI layer, the volume of the turbulent region V_T is computed as a function of ω_{th}, as shown in figure 3. The threshold ω_{th} shown in the figure is normalized as $\hat{\omega}_{th} = \omega_{th}/\langle\omega\rangle_c$, where the subscript c denotes the value taken at $y = 0.5\delta$, which is located in the turbulent core region. The volume of

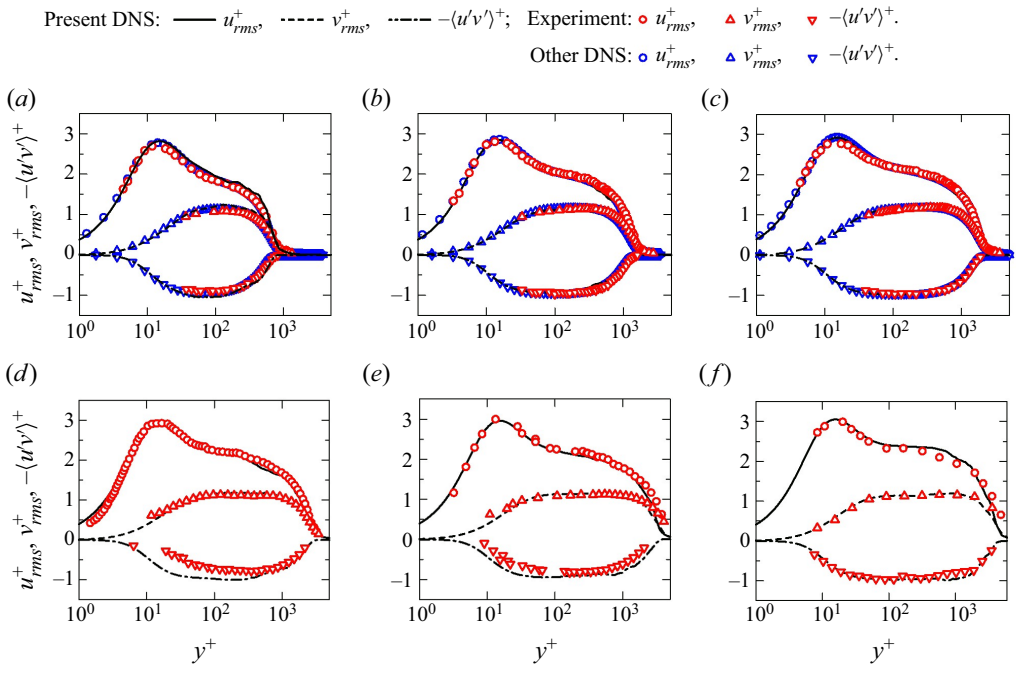

Figure 2. Vertical profiles of r.m.s. values of streamwise and vertical velocity fluctuations and Reynolds stress in cases (*a*) B02 ($Re_\theta = 2000$), (*b*) B04 ($Re_\theta = 4000$), (*c*) B06 ($Re_\theta = 6000$), (*d*) B08 ($Re_\theta = 8000$), (*e*) B10 ($Re_\theta = 10\,000$), and (*f*) B13 ($Re_\theta = 13\,000$). The DNS results are compared with: experimental results (*a*) $Re_\theta = 2100$ (Osaka, Kameda & Mochizuki 1998), (*b*) $Re_\theta = 4400$ (Osaka *et al.* 1998), (*c*) $Re_\theta = 6040$ (Osaka *et al.* 1998), (*d*) $Re_\theta = 8100$ ($Re_\tau = 2500$; Carlier & Stanislas 2005), (*e*) $Re_\theta = 11\,500$ ($Re_\tau = 4000$; Carlier & Stanislas 2005), (*f*) $Re_\theta = 13\,000$ ($Re_\tau = 4336$; De Graaff & Eaton 2000); and previous spatial DNS results (*a*) $Re_\theta = 1986$ ($Re_\tau = 671$; Schlatter & Örlü 2012), (*b*) $Re_\theta = 2000$ ($Re_\tau = 1271$; Schlatter & Örlü 2012), (*c*) $Re_\theta = 4000$ ($Re_\tau = 1848$; Sillero, Jiménez & Moser 2013), at similar Reynolds numbers.

the turbulent region is also normalized, as $\hat{V}_T = V_T/(L_x L_z \delta)$. Figure 3 also shows the derivative of $\hat{V}_T$, $\mathrm{d}\hat{V}_T/\mathrm{d}\log(\hat{\omega}_{th})$. The profile of $\hat{V}_T$ is similar to profiles obtained in previous studies (da Silva *et al.* 2014; Jahanbakhshi, Vaghefi & Madnia 2015; Watanabe *et al.* 2015). The turbulent volume largely increases for $\hat{\omega}_{th} < 10^{-4}$ as $\hat{\omega}_{th}$ decreases, because the non-turbulent region has very small vorticity magnitude, which is often associated with the numerical error. On the other hand, $\hat{V}_T$ hardly changes within the range $10^{-3} < \hat{\omega}_{th} < 10^{-2}$, which indicates that the location of the isosurface $\omega = \omega_{th}$ hardly changes with ω_{th} within this range. In the present study, $\hat{\omega}_{th} = 10^{-2.5}$ shown as a vertical dot-dash line in figure 3 is used to detect the irrotational boundary.

This method based on the threshold dependence of the turbulent volume has been used widely for choosing the isosurface value for studying the TNTI layer (Taveira *et al.* 2013; Jahanbakhshi *et al.* 2015). Statistics near the TNTI layer are often computed as functions of the distance from the isosurface $\omega = \omega_{th}$ (Bisset *et al.* 2002). Previous studies have shown that the statistics near the TNTI layer hardly change with a small change of ω_{th} if ω_{th} is chosen based on the ω_{th} dependence of the turbulent volume (Taveira *et al.* 2013; Watanabe *et al.* 2018*b*; Watanabe, da Silva & Nagata 2019*a*). We have also tested different values of ω_{th} within the range $10^{-3} < \hat{\omega}_{th} < 10^{-2}$ with the present DNS database, and

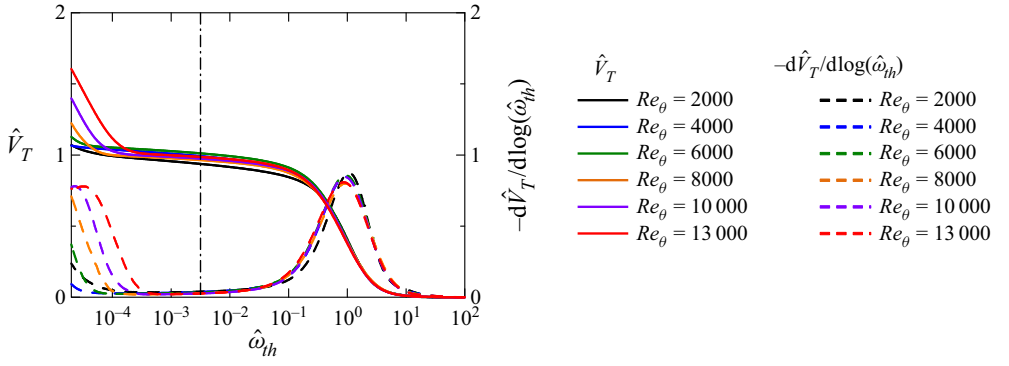

Figure 3. The normalized turbulent volume $\hat{V}_T$ plotted against the normalized threshold $\hat{\omega}_{th}$ used for detecting turbulent fluids. Here, $\mathrm{d}\hat{V}_T/\mathrm{d}\log(\hat{\omega}_{th})$ is also plotted, with dashed lines. A vertical dot-dash line indicates the threshold value used in this study to detect the irrotational boundary.

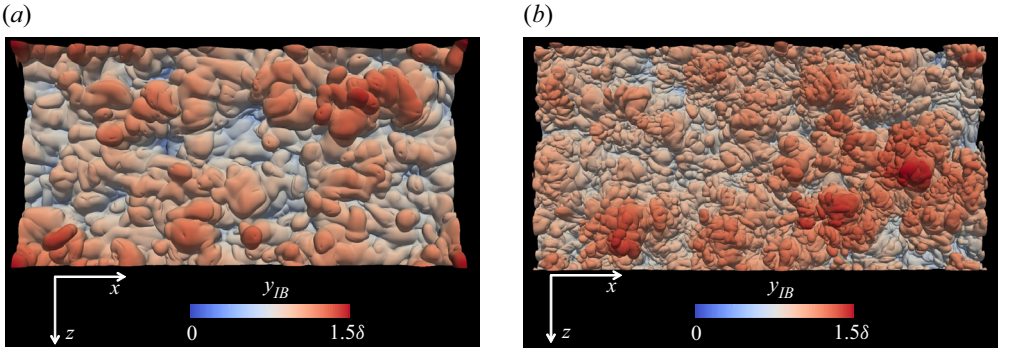

Figure 4. Visualization of an irrotational boundary forming at the outer edge of the TNTI layer for (*a*) case B02 ($Re_\theta = 2000$), and (*b*) case B13 ($Re_\theta = 13\,000$). Colour represents the height of irrotational boundary y_{IB}.

have found that the detected isosurface location and the statistics near the TNTI layer are insensitive to the threshold.

Figure 4 visualizes the irrotational boundary coloured by the height of the irrotational boundary from the wall, y_{IB}, for $Re_\theta = 2000$ and 13 000. The irrotational boundary in the present DNS looks very smooth and similar to those detected in free shear flows (Watanabe, Riley & Nagata 2017*b*; Nagata *et al.* 2018), while some previous DNS of the TBL with coarser grids ($\Delta_x^+ \approx 9$) showed spiky patterns of the irrotational boundary, as discussed in Zhang *et al.* (2018) and Watanabe *et al.* (2018*b*). A folded shape of the irrotational boundary can be characterized by a wide range of length scales of turbulent motions that appear under the TNTI layer. Therefore, the small-scale structures appear in $Re_\theta = 13\,000$ rather than in $Re_\theta = 2000$. Figure 5 shows a colour contour of enstrophy $\omega^2/2$ and the irrotational boundary on an x–y plane. The geometries of the irrotational boundary are different for $Re_\theta = 2000$ and 13 000, where the irrotational boundary is more folded for higher Re_θ, but flatter for lower Re_θ. The mean height of the irrotational boundary is approximately 0.9δ for all the Reynolds numbers, and the irrotational boundary appears for $0.4\delta \leq y \leq 1.4\delta$, which is consistent with an intermittency factor profile in spatially developing TBLs (Borrell & Jiménez 2016).

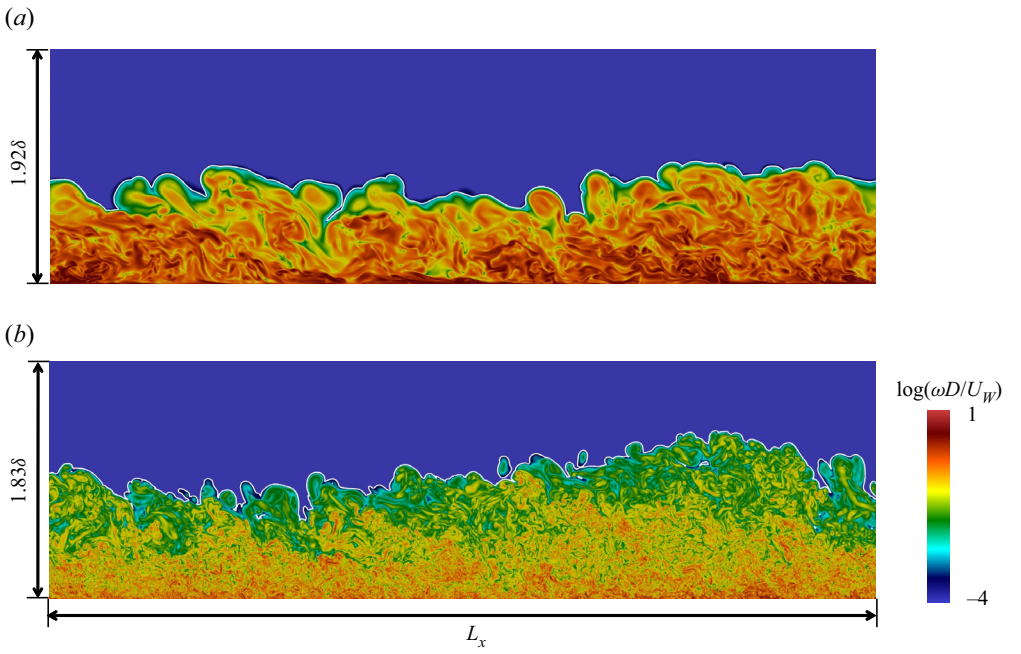

Figure 5. Two-dimensional snapshots of temporally developing boundary layers on the x–y plane. The colour represents vorticity magnitude $\log(\omega D/U_W)$, and the irrotational boundary is visualized with the white line. The wall is moving in the x direction (from left to right): (a) case B02 ($Re_\theta = 2000$), (b) case B13 ($Re_\theta = 13\,000$).

The TNTI layer can be studied with statistics conditioned on the distance from the irrotational boundary. The local coordinate y_I is defined so that the irrotational boundary is located at $y_I = 0$, and the direction of y_I is normal to the irrotational boundary, pointing into the non-turbulent region. Here, the normal direction of the irrotational boundary can be obtained as $\boldsymbol{n} = -\nabla\omega^2/|\nabla\omega^2|$, and the non-turbulent and turbulent regions are represented by $y_I > 0$ and $y_I < 0$, respectively. The conditional statistics are obtained as functions of y_I, where samples of the statistics for $y_I > 0$ and $y_I < 0$ are taken only from non-turbulent and turbulent flow points, respectively, even though the local coordinate y_I intersects more than one irrotational boundary point. Further details of the computation of the conditional statistics can be found in our previous papers (Nagata *et al.* 2018; Watanabe *et al.* 2018*b*, 2019*a*; Zhang *et al.* 2018). The average taken on the local coordinate is denoted by $\langle\cdot\rangle_I$.

3.2. *Mean thickness of the TNTI layer and sublayers*

The TNTI layer can be defined as a region where the vorticity magnitude is adjusted between the turbulent and non-turbulent regions (da Silva *et al.* 2014). Therefore, the TNTI layer can be characterized by a large gradient of vorticity magnitude in the TNTI normal direction. The mean thickness of the TNTI layer is quantified based on the mean vorticity magnitude $\langle\omega\rangle_I$, as shown in figure 6(a) following our previous studies (Watanabe *et al.* 2018*a*; Zhang *et al.* 2018). Figure 6(a) also shows the derivative of $\langle\omega\rangle_I$, $\langle\omega\rangle_I' = -\mathrm{d}\langle\omega\rangle_I/\mathrm{d}y_I$, where the mean thickness of the TNTI layer, δ_{TNTI}, is defined as the distance from $y_I = 0$ to the location where $\langle\omega\rangle_I'$ reaches 20 % of its maximum value. The mean thickness of the TNTI layer was also quantified by fitting an error function to the

conditional statistics in the previous study, and both methods result in a similar value of the mean thickness of the TNTI layer (Watanabe *et al.* 2018*a*).

Figure 6(*b*) shows the conditional profiles of Kolmogorov scale defined as $\eta_I = \nu^{3/4}\langle\varepsilon\rangle_I^{-1/4}$ and Taylor microscale defined as $\lambda_I = \sqrt{10k_I/(\langle\varepsilon\rangle_I\nu)}$, where k_I is the turbulent kinetic energy defined as $k_I = (\langle u_i^2\rangle_I - \langle u_i\rangle_I^2)/2$. The distance from the irrotational boundary, y_I, is normalized by δ_{TNTI}. These two scales are quite large in the non-turbulent region, then decrease rapidly from the non-turbulent region to the turbulent region, and tend to be constant in the turbulent core region. The turbulent statistics at $y_I/\delta_{TNTI} = -2$ shown by the vertical dot-dash line are used as reference quantities for investigating the TNTI layer. The choice $y_I/\delta_{TNTI} = -2$ ensures the 'same' distance from the TNTI layer for different Reynolds numbers. Hereafter, the subscript '*TI*' indicates the statistics taken at this location. The corresponding turbulent Reynolds number $Re_{\lambda.TI} = \lambda_{TI}\sqrt{(2/3)k_{TI}}/\nu$ near the TNTI layer at $y_I/\delta_{TNTI} = -2$ is also calculated, and shown in table 3.

The TNTI layer contains two sublayers, the viscous superlayer (VSL) and the turbulent sublayer (TSL). These inner structures of the TNTI layer can be distinguished by vorticity dynamics (van Reeuwijk & Holzner 2014; Taveira & da Silva 2014). The conditional averages of the production term $\langle P_\omega\rangle_I$ and the viscous diffusion term $\langle D_\omega\rangle_I$ in the enstrophy transport equation can be used for identifying the VSL and TSL (Taveira & da Silva 2014; Zhang *et al.* 2018). The enstrophy transport equation is

$$\frac{\mathrm{D}(\omega^2/2)}{\mathrm{D}t} = \omega_i S_{ij}\omega_j + \nu\,\nabla^2(\omega^2/2) + \nu\,\nabla\omega_i\cdot\nabla\omega_i. \tag{3.1}$$

The three terms on the right-hand side are the production $\langle P_\omega\rangle_I$, viscous diffusion $\langle D_\omega\rangle_I$ and viscous dissipation $\langle\varepsilon_\omega\rangle_I$, respectively. The production term $\langle P_\omega\rangle_I$ and the viscous diffusion term $\langle D_\omega\rangle_I$ are almost 0 at the irrotational boundary ($y_I = 0$), then they increase from the irrotational boundary towards the turbulent region. The mean viscous diffusion term is larger than the production term near the irrotational boundary, where the mean thickness of the VSL, δ_{VSL}, can be identified as the region where $\langle D_\omega\rangle_I > \langle P_\omega\rangle_I$ near the irrotational boundary (Taveira & da Silva 2014; Jahanbakhshi *et al.* 2015; Watanabe *et al.* 2015; Zhang *et al.* 2018). Then it is easy to measure the mean thickness of the TSL, δ_{TSL}, which is considered as the buffer region between the VSL and the turbulent core region. Within the TSL, the inviscid process (production term) has a larger contribution to the increase of the enstrophy (da Silva *et al.* 2014). The mean thicknesses of the TNTI layer (δ_{TNTI}), VSL (δ_{VSL}) and TSL (δ_{TSL}) normalized by Kolmogorov scale η_{TI} and Taylor microscale λ_{TI} near the TNTI layer are plotted in figures 7(*a*) and 7(*b*), respectively. From figure 7(*a*), we can see that the average thickness of δ_{TNTI} is approximately $15.7\eta_{TI}$, δ_{VSL} is approximately $4.6\eta_{TI}$, and δ_{TSL} is approximately $11.1\eta_{TI}$ for all the Reynolds numbers. However, $\delta_{TNTI}/\lambda_{TI}$, $\delta_{TSL}/\lambda_{TI}$ and $\delta_{VSL}/\lambda_{TI}$ all decrease with the increase of the Reynolds number, as shown in figure 7(*b*). These results are consistent with a previous study (Silva *et al.* 2018), in which the thickness of the TNTI layer and sublayers normalized by the Kolmogorov scale is almost constant for the different Reynolds numbers, while the thickness normalized by λ decreases with $Re_\lambda^{-1/2}$ in jets and shear-free turbulence. Hereafter, we assume that the mean thicknesses of the TNTI layer and VSL are approximately $15\eta_{TI}$ and $5\eta_{TI}$, for convenience. Our result is also consistent with the results from Jahanbakhshi (2021), where δ_{VSL} is approximately 5η, and δ_{TNTI} is of the order of $O(10\eta)$ at $Re_\tau \approx 600$ in the spatial TBL.

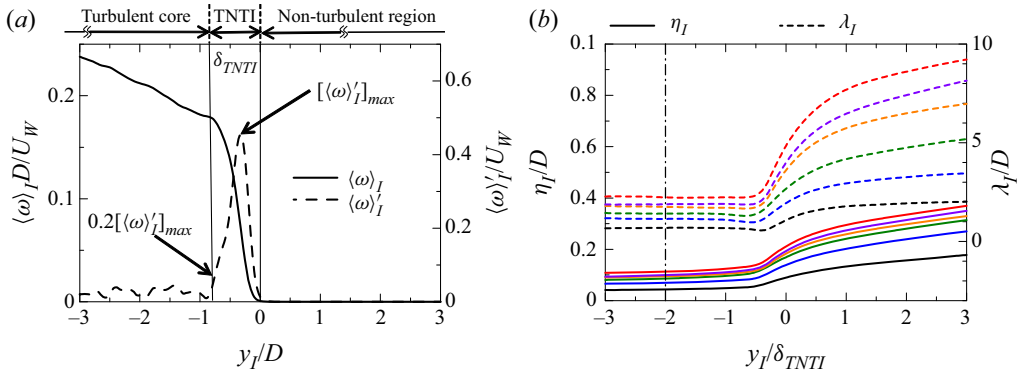

Figure 6. (*a*) Conditional mean vorticity and its derivative with respect to y_I for case B02. (*b*) Conditional profiles of Kolmogorov length scale η_I and Taylor microscale λ_I defined with conditional averages. The line colours represent the Reynolds numbers as shown in figure 3. The vertical dot-dash line shows $y_I/\delta_{TNTI} = -2$, where the reference scales are taken for studying the TNTI layer.

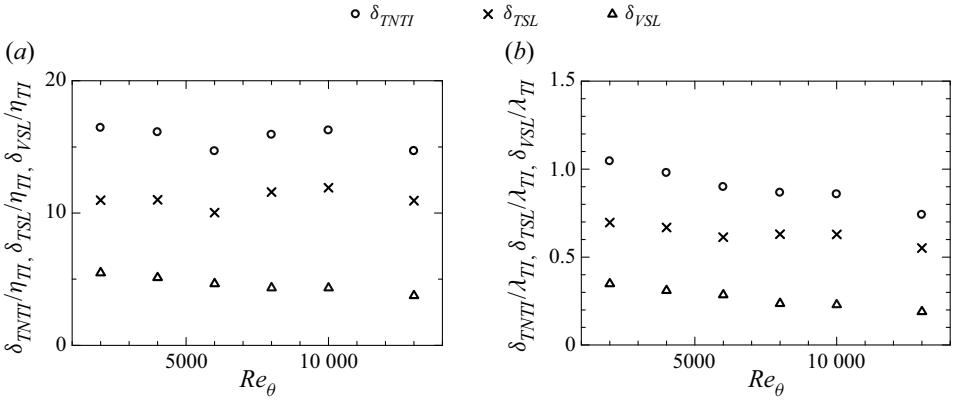

Figure 7. The mean thickness of the TNTI layer, the viscous superlayer (VSL), and the turbulent sublayer (TSL) normalized by (*a*) Kolmogorov scale η_{TI}, and (*b*) Taylor microscale λ_{TI}, at $y_I/\delta_{TNTI} = -2$.

Case	B02	B04	B06	B08	B10	B13
Re_θ	2000	4000	6000	8000	10 000	13 000
$Re_{\lambda.TI}$	64	70	69	87	93	102

Table 3. Turbulent Reynolds number $Re_{\lambda.TI}$ of the turbulent flow near the TNTI layer at $y_I/\delta_{TNTI} = -2$.

3.3. *The turbulent statistics near and within the TNTI layer*

Figure 8(*a*) shows the conditional mean vorticity magnitude $\langle\omega\rangle_I$ normalized by wall velocity U_W and trip wire diameter D with y_I normalized by η_{TI}. The mean vorticity magnitude in figure 8(*a*) decreases with the increase of Reynolds number. In the meantime, the vertical profiles of the average of ω taken only from the turbulent region, $\langle\omega\rangle_T$, in comparison with the conventional average $\langle\omega\rangle$, are shown in figure 8(*b*). Because turbulent fluids have $\omega \geq \omega_{th}$, $\langle\omega\rangle_T$ does not decrease to 0 for large y, unlike $\langle\omega\rangle$, which decreases to 0 for large y. In the figure, the location of the mean irrotational boundary height is

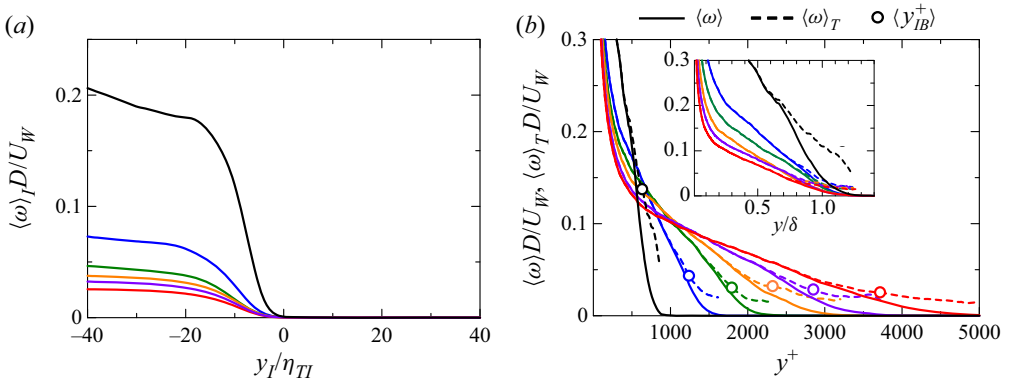

Figure 8. (*a*) Conditional mean profile of vorticity magnitude normalized by wall velocity U_W and trip wire diameter D plotted with respect to y_I/η_{TI}. (*b*) Vertical profiles of the mean vorticity magnitude computed only from turbulent fluids, $\langle\omega\rangle_T$, and the conventional average of ω based on the spatial average on x–z planes, $\langle\omega\rangle$. The circle symbols represent the mean irrotational boundary height, and the inset shows $\langle\omega\rangle$, $\langle\omega\rangle_T$ normalized by the boundary layer thickness δ. The line colours represent the Reynolds numbers as shown in figure 3.

marked by circles. In the intermittent region, where $\langle\omega\rangle$ differs from $\langle\omega\rangle_T$, $\langle\omega\rangle_T$ tends to be independent of large y^+ at high Reynolds numbers. On the other hand, $\langle\omega\rangle_T$ in the intermittent region still rapidly decreases with y^+ for low Reynolds numbers. This strong dependence of $\langle\omega\rangle_T$ on y^+ can be seen near the wall for all Reynolds numbers. Since the ratio between y and δ_ν is small in the intermittent region at a low Reynolds number, the intermittent region can be influenced by the wall, and $\langle\omega\rangle_T$ in the intermittent region depends strongly on y. On the other hand, because y/δ_ν in the intermittent region is large at high Reynolds numbers, the intermittent region in this case is less influenced by the strong mean shear near the wall. This results in the weak dependence of $\langle\omega\rangle_T$ on y in the intermittent region.

Figure 9(*a*) shows $\langle\omega\rangle_I$ normalized by vorticity ω_{TI} at $y_I = -2\delta_{TNTI}$. The mean vorticity jump at different Reynolds numbers collapses well within the TNTI layer (y_I from 0 to approximately $15\eta_{TI}$) in figure 9(*a*). The conditional averages of second invariant of velocity gradient tensor $\langle Q\rangle_I$ are plotted in figure 9(*b*). Here, Q is defined as $Q = (\omega_{ij}\omega_{ij} - S_{ij}S_{ij})/2$, with $\omega_{ij} = (\partial u_i/\partial x_j - \partial u_j/\partial x_i)/2$ and $S_{ij} = (\partial u_j/\partial x_i + \partial u_i/\partial x_j)/2$. We also normalize $\langle Q\rangle_I$ by the mean strain product taken at $y_I = -2\delta_{TNTI}$, which is denoted as s^2_{TI}. In this figure, the profiles for different Reynolds numbers also collapse together. In these profiles, we can see that the vorticity is weaker than strain ($Q < 0$) within the VSL, and stronger than strain ($Q > 0$) within the TSL, as also found in other free shear flows. Here, figures 9(*a*) and 9(*b*) both indicate that the turbulent characteristics taken at $y_I = -2\delta_{TNTI}$ well characterize the statistics near the TNTI layer. The DNS results for a temporally developing planar jet with jet Reynolds number 10 000 (Watanabe *et al.* 2019*b*) are also compared in figure 9. The shape and magnitude of the conditional mean vorticity and the second invariant of velocity gradient tensor are similar between the jet and TBL when they are normalized by η_{TI}.

Figure 10(*a*) shows the conditional mean streamwise velocity $\langle u\rangle_I$ normalized by the friction velocity u_τ. The conditional mean velocity is very small and almost constant within the VSL, then it increases rapidly in the TSL, and the mean velocity is still increasing gradually in the turbulent core region. However, the mean streamwise velocity is flat within the VSL, which indicates that the mean shear is absent within the VSL.

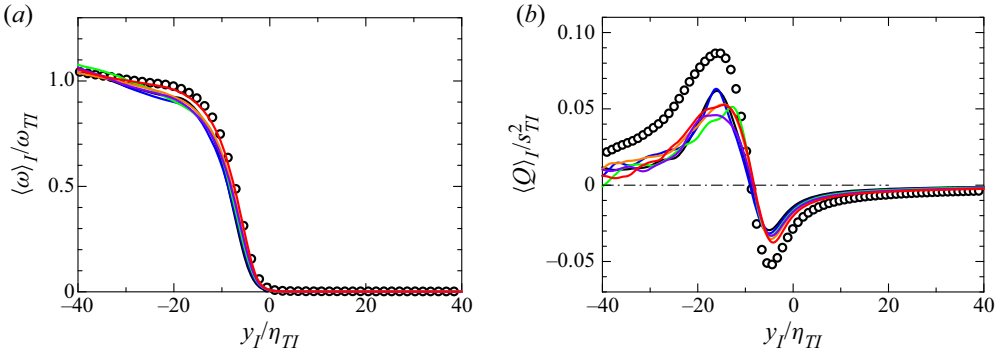

Figure 9. The normalized conditional mean profiles of (*a*) mean vorticity magnitude $\langle\omega\rangle_I/\omega_{TI}$, and (*b*) the second invariant of velocity gradient tensor $\langle Q\rangle_I/s_{TI}^2$, where ω_{TI} and s_{TI}^2 represent $\langle\omega\rangle_I$ and $\langle S_{ij}S_{ij}\rangle_I$ calculated at $y_I/\delta_{TNTI} = -2$, respectively. The line colours represent the Reynolds numbers as shown in figure 3. The circle symbols represent the data of a turbulent planar jet with the jet Reynolds number 10 000 (Watanabe *et al.* 2019*b*).

In this study, $\langle u\rangle_I$ is qualitatively different from the result by Eisma *et al.* (2015), which is well approximated by their Z-shape model. The Z-shape model is characterized by sudden changes of the mean velocity gradient at the boundaries among the turbulent core region, the TNTI layer and the non-turbulent region. The present results confirm that $\langle u\rangle_I$ increases from the TNTI layer to the turbulent core region without a significant change of the mean velocity gradient. It seems that this difference is due to different definitions of the local coordinate used for the conditional statistics. Eisma *et al.* (2015) considered the local coordinate taken in the wall-normal direction, while y_I in this study is taken in the interface normal direction. It was also shown that the Z-shape model for $\langle u\rangle_I$ is valid in a turbulent planar jet if the local coordinate is taken in the transverse direction of the jet (Watanabe *et al.* 2014). These results indicate that the conditional mean velocity profile near the TNTI layer is sensitive to the definition of the local interface coordinate. The inset of figure 10(*a*) shows $\langle u\rangle_I$ normalized by $u_{rms.TI}$, which is the r.m.s. of streamwise velocity u_{rmsI} at $y_I/\delta_{TNTI} = -2$. Here, u_{rmsI} is defined as $\sqrt{\langle u^2\rangle_I - \langle u\rangle_I^2}$. The velocity jump of $\langle u\rangle_I$ across the TNTI layer is approximately one order of $u_{rms.TI}$. The temporally developing planar jet with jet Reynolds number 10 000 (Watanabe *et al.* 2019*b*) is also compared in figure 10(*a*), where the profiles are similar for the jet and TBL when y_I is normalized by η_{TI}. Even though it seems from figure 10(*a*) that the mean shear exists within and near the TNTI layer, how significantly the mean shear affects the TNTI layer is still not clear.

Figure 10(*b*) shows the conditional mean of vertical velocity, $\langle v\rangle_I/u_\tau$, which becomes positive in the turbulent core region and negative in the non-turbulent region. This profile is consistent with previous studies on a spatially developing TBL (Eisma *et al.* 2015) and a turbulent planar jet (Watanabe *et al.* 2014). Negative $\langle v\rangle_I/u_\tau$ in the non-turbulent region is expected from large-scale motions, such as sweeps (Pope 2000) in TBLs, which are expected to be related to the engulfment. The engulfment process can draw the non-turbulent fluids towards the turbulent region directly, where the valley structures appear on the TNTI with the negative $\langle v\rangle_I$ in the non-turbulent region. The profile of $\langle v\rangle_I$ is also consistent with experimental results obtained for the interface detected with kinetic energy (Chauhan *et al.* 2014*a*; de Silva *et al.* 2017). The mean vertical velocity defined with an average taken on a horizontal plane, $\langle v\rangle$, is zero at any locations in the temporally developing TBLs, unlike in spatially developing TBLs. However, the conditional profile

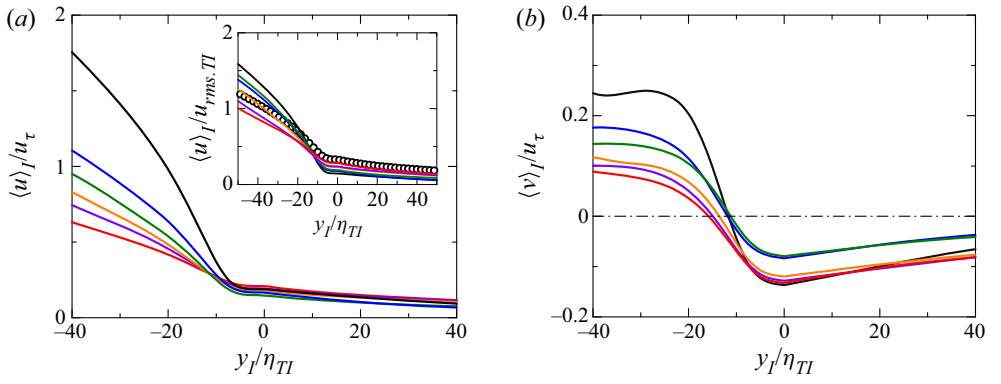

Figure 10. (*a*) Conditional mean streamwise velocity $\langle u\rangle_I$ and (*b*) conditional mean vertical velocity $\langle v\rangle_I$, normalized by the friction velocity u_τ. The inset in (*a*) shows $\langle u\rangle_I$ normalized by the r.m.s. streamwise velocity fluctuation $u_{rms.TI}$ calculated at $y_I/\delta_{TNTI} = -2$. The circle symbols represent the data of a turbulent planar jet with jet Reynolds number 10 000 (Watanabe *et al.* 2019*b*).

of $\langle v\rangle_I$ is consistent between temporal and spatial TBLs, and the non-turbulent fluid motions in the vicinity of the interface are similar in both temporal and spatial TBLs. These non-turbulent fluid motions are related to a part of the entrainment process, and the temporal simulation well captures the process by which the non-turbulent fluid is transferred towards the TNTI in the intermittent region of spatially developing TBLs. Also, the changes in the conditional mean streamwise and vertical velocities across the TNTI layer are of the same order as in previous studies (Chauhan *et al.* 2014*a*; Eisma *et al.* 2015).

The conditional r.m.s. values of streamwise velocity u_{rmsI}, wall-normal velocity v_{rmsI} and spanwise velocity w_{rmsI} are shown in figure 11. It should be noticed again that the conditional r.m.s. of streamwise velocity u_{rmsI} is defined as $\sqrt{\langle u^2\rangle_I - \langle u\rangle_I^2}$; v_{rmsI} and w_{rmsI} are calculated in the same way as u_{rmsI}. The low Reynolds number case has a larger r.m.s. value for all velocity components in the turbulent region, but the r.m.s. velocity fluctuations tend to be independent of the Reynolds number for high Reynolds numbers. This might be because the production term of the turbulent kinetic energy budget is almost 0 for large y^+ (Smits, McKeon & Marusic 2011). As we mentioned before, the height y_{IB} of the irrotational boundary is approximately 0.9δ, namely $y^+_{IB} \approx 0.9Re_\tau$, which is why the r.m.s. fluctuations of the three velocity components are similar to each other for high Reynolds numbers. The jumps of r.m.s. velocity fluctuations near the TNTI layer in the present DNS are of the same order in their experimental results (Chauhan *et al.* 2014*a*), where the TBLs are investigated experimentally between $Re_\tau = 1230$ and $Re_\tau = 14\,500$.

3.4. *The shear effects near and within the TNTI layer*

As shown in figure 10, the mean shear exists within and near the TNTI layer, where we investigate how significantly the mean shear affects the TNTI layer. Therefore, the conditional shear parameter defined as $S^*_I = \langle\partial u/\partial y\rangle_I\langle k\rangle_I/\langle\varepsilon\rangle_I$ based on the conditional mean streamwise velocity derivative is calculated for evaluating the shear effects on the energy-containing eddies near the TNTI. The shear parameter is defined as the ratio between the decay time of energy-containing eddies and the shear deformation time (Corrsin 1958). Figure 12(*a*) shows that the conditional shear parameter is approximately

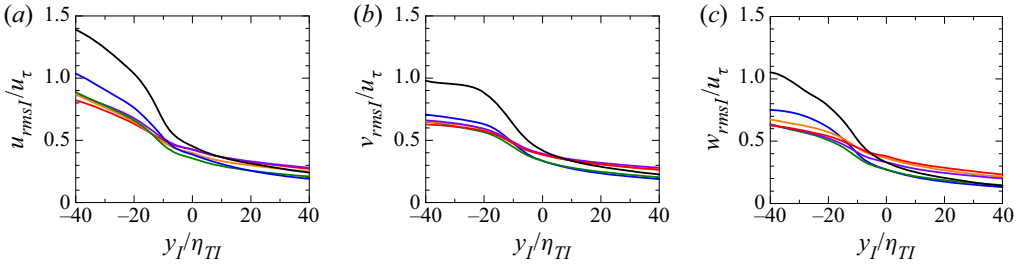

Figure 11. Conditional r.m.s. velocity fluctuations: (*a*) streamwise velocity, (*b*) wall-normal velocity, and (*c*) spanwise velocity. The line colours represent the Reynolds numbers as shown in figure 3.

4 in the turbulent core region for all the Reynolds numbers, and the value of S_I^* is within the typical range (from 3 to 6) in turbulent shear flows (Pope 2000). The conditional shear parameter decreases from the TSL towards the irrotational boundary (y_I from 15 to 0). The value of the shear parameter indicates that the shear effects do exist near and within the TNTI layer, but are not very significant on the large-scale eddies. Furthermore, the value of the shear parameter within the TNTI layer is in the typical range of shear flows (Pope 2000).

The conditional shear-to-vorticity ratio S_I/ω_I' is shown in figure 12(*b*), where the conditional mean shear S_I is defined as $S_I = \langle \partial u/\partial y \rangle_I$, and the conditional fluctuation ω_I' is defined as $\omega_I' = \sqrt{\langle \omega_I^2 \rangle - \langle \omega_I \rangle^2}$. This ratio indicates the relative shear effects on the small-scale motions near the TNTI. If S_I/ω_I' is much smaller than 1, then the small-scale vortices are decoupled from the mean shear and become roughly isotropic (Jiménez 2013). As shown in figure 12(*b*), S_I/ω_I' under the TNTI layer is approximately 0.1–0.2. These values are so small that the mean shear effects on small-scale motions are weak. The Reynolds number dependence can still be found in this figure: the results with a higher Reynolds number have a lower value of S_I/ω_I', which means that the vortices tend to be more isotropic with the increase of Reynolds number. This observation is similar to that found by computing conventional average S/ω' in the outer layer ($y = 0.6\delta$) (Jiménez 2013). Finally, because the irrotational boundary ($y_I = 0$) is detected by a vorticity magnitude isosurface, the vorticity fluctuation is close to zero near the irrotational boundary, which causes the large value of S_I/ω_I' near the irrotational boundary.

In general, the boundary layer thickness δ represents the characteristic length scale of large-scale motions (Pope 2000), and η_{TI} indicates the smallest scale of the turbulence near the TNTI layer. Figure 13(*a*) shows the ratio between η_{TI} and δ against the Reynolds number Re_θ. The red dot-dash line represents $C_1\, Re_\theta^{-3/4}$, where $C_1 = 2.3$ is a constant obtained from the present DNS data with $Re_\theta \geq 4000$. It is a scaling law for homogeneous isotropic turbulence (HIT), $\eta/l_0 \sim Re^{-3/4}$, where l_0 is the integral length scale that represents the length scale of large-scale motions for homogeneous isotropic turbulence (Pope 2000). It can be seen clearly that the results at relatively high Reynolds numbers ($Re_\theta = 6000$–$13\,000$) agree well with the red dot-dash line. However, the results for $Re_\theta = 2000$ and 4000 are lower than this line, especially for $Re_\theta = 2000$. It is expected that the wall has more significant influences on the TNTI layer at lower Reynolds numbers, which might explain the departure from $\eta/\delta \sim Re_\theta^{-3/4}$.

Figure 13(*b*) shows the second invariants of the anisotropy tensors of the Reynolds stress and vorticity in the turbulent region near the TNTI, $B2_{TI}$ and $V2_{TI}$. These invariants are

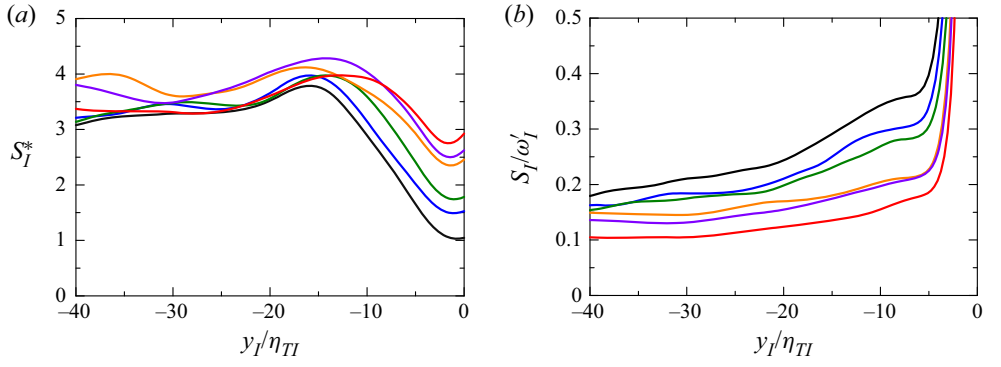

Figure 12. (*a*) Conditional shear parameter defined as $S_I^* = \langle \partial u/\partial y \rangle_I \langle k \rangle_I / \langle \varepsilon \rangle_I$ near the TNTI layer. (*b*) Conditional shear-to-vorticity ratio S_I/ω_I' near the TNTI layer. The line colours represent the Reynolds numbers as shown in figure 3.

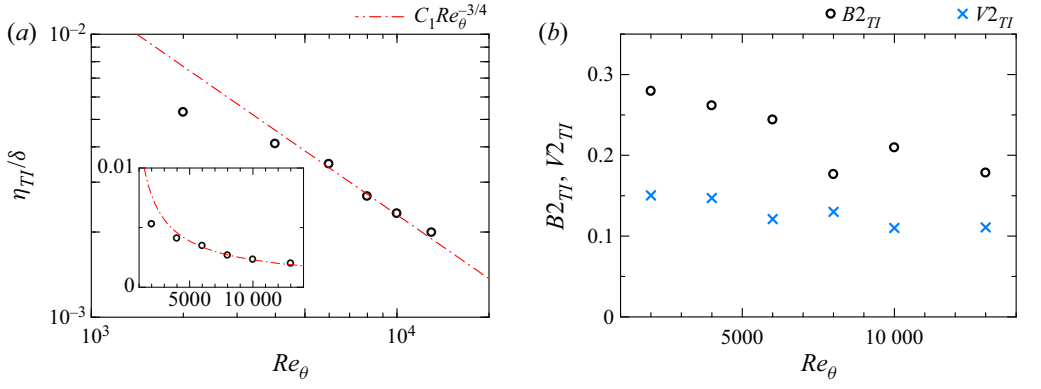

Figure 13. (*a*) The Re_θ dependence of the length scale ratio between the Kolmogorov scale η_{TI} and boundary layer thickness δ at $y_I/\delta_{TNTI} = -2$. The inset shows the corresponding plot with a linear scale. (*b*) The second invariants of the anisotropy tensor of Reynolds stress and vorticity for turbulence near the TNTI, which are denoted $B2_{TI}$ and $V2_{TI}$, respectively.

defined as $B2_{TI} = (3\langle b_{ij}\rangle_{TI}\langle b_{ij}\rangle_{TI}/2)^{1/2}$ and $V2_{TI} = (3\langle v_{ij}\rangle_{TI}\langle v_{ij}\rangle_{TI}/2)^{1/2}$, respectively, with the anisotropy tensors of the Reynolds stress and vorticity:

$$\langle b_{ij}\rangle_{TI} = \frac{\langle u_i u_j\rangle_{TI} - \langle u_i\rangle_{TI}\langle u_j\rangle_{TI}}{\langle u_k u_k\rangle_{TI} - \langle u_k\rangle_{TI}\langle u_k\rangle_{TI}} - \frac{1}{3}\delta_{ij}, \tag{3.2}$$

$$\langle v_{ij}\rangle_{TI} = \frac{\langle \omega_i \omega_j\rangle_{TI}}{\langle \omega_k \omega_k\rangle_{TI}} - \frac{1}{3}\delta_{ij}. \tag{3.3}$$

Here, δ_{ij} is Kronecker's delta. The values of $B2_{TI}$ and $V2_{TI}$ indicate the anisotropy related to the large- and small-scale turbulent motions under the TNTI, respectively. The invariants are equal to 1 and 0 for complete anisotropy and isotropy, respectively. In the figure, $B2_{TI}$ is larger than $V2_{TI}$, indicating that large-scale motions are more anisotropic compared with small-scale ones. Higher isotropy for smaller scales is related to the weak mean shear effects for small-scale motions as examined with S_I/ω_I' in figure 12(*b*). As expected from the above discussion, both invariants decrease with the Reynolds number, and the flow under the TNTI becomes close to isotropic turbulence. This behaviour is

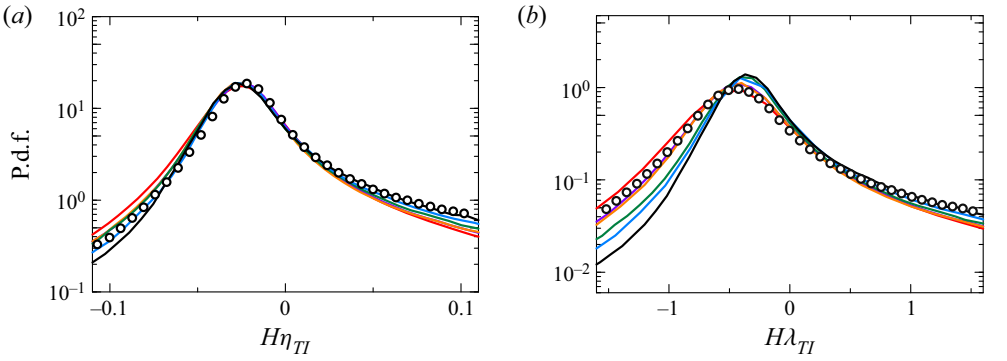

Figure 14. The p.d.f.s of the mean curvature of the irrotational boundary normalized by (*a*) Kolmogorov length scale η_{TI}, and (*b*) Taylor microscale λ_{TI}. The line colours represent the Reynolds numbers as shown in figure 3. The circle symbols represent the data of a turbulent planar jet with jet Reynolds number 10 000 (Watanabe *et al.* 2019*b*).

related to the departure from the scaling law for HIT at the low Reynolds numbers as shown in figure 13(*a*). A similar observation was made by Jiménez (2013), where the turbulence motions in the outer layer become more isotropic with the increase of Reynolds number in channel flow.

3.5. *The geometry of the irrotational boundary*

The probability density function (p.d.f.) of the mean curvature $H = (1/2)\nabla \cdot \boldsymbol{n}$ of the irrotational boundary is shown in figure 14, where the p.d.f. is normalized by the Kolmogorov length scale η_{TI} in figure 14(*a*), and by the Taylor microscale λ_{TI} in figure 14(*b*). The positive/negative value of H indicates the concave/convex region in the top view of the TBL shown in figure 4. The profiles of p.d.f.s normalized by η_{TI} are similar with different Reynolds numbers ($Re_\theta = 2000$–$13\,000$); in particular, the locations and values of peaks in the p.d.f.s collapse together for all the Reynolds numbers. The p.d.f. normalized by λ_{TI} depends strongly on the Reynolds number, as confirmed by the variation of the peak value and location of the p.d.f. with the Reynolds number. Therefore, the mean curvature of the irrotational boundary is well characterized by the Kolmogorov scale η_{TI}. The DNS results for a temporally developing planar jet with jet Reynolds number 10 000, ($Re_\lambda = 97$) (Watanabe *et al.* 2019*b*) are also compared in figure 14(*a*). The p.d.f. of the mean curvature hardly differs for the jet and TBL when they are normalized by η_{TI}. The p.d.f. has a peak at $H\eta_{TI} \approx -0.025$, which indicates that a large part of the irrotational boundary has curvature radius approximately $40\eta_{TI}$. The length $40\eta_{TI}$ is the typical length scale of velocity gradients in the outer logarithmic layer or outer layer (Jiménez 2013). On the other hand, the mean curvature p.d.f. normalized by λ_{TI} for the jet ($Re_\lambda = 97$) collapses with $Re_\theta = 10\,000$ ($Re_{\lambda.TI} = 90$) for the TBL but differs for lower Reynolds numbers, which also indicates that the p.d.f. normalized by λ_{TI} depends on the Reynolds number. With flow visualization, previous studies observed small-scale vortex tubes within the TNTI layer, and the interface forms around them (da Silva, Dos Reis & Pereira 2011). The curvature of the TNTI is expected to be related to the diameter of the vortices or the curvature radius of the vortex axis since both the curvature radius of the TNTI and the length scale of vortex tubes scale with the Kolmogorov scale. This is geometrical

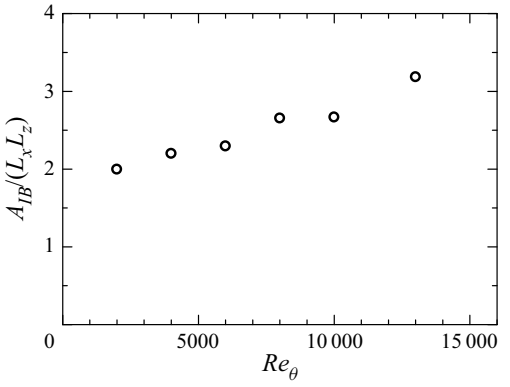

Figure 15. The Re_θ dependence of surface area of the irrotational boundary A_{IB}.

information about the irrotational boundary, which is expected to be related to the turbulent structure with a similar length scale beneath the irrotational boundary.

Figure 15 shows the surface area of irrotational boundary A_{IB} normalized by L_xL_z. Here, $A_{IB}/(L_xL_z)$ is around 2–4 and increases with the Reynolds number because of the complex shape of the irrotational boundary at high Re_θ, as shown in figure 4. The previous study (Meneveau & Sreenivasan 1990) suggested that the surface area is related to the fractal dimension of the irrotational boundary because the complex shape is caused by the multiscale turbulent motions under the TNTI. Here, the box-counting analysis is conducted to investigate the fractal characteristics of the TNTI (Prasad & Sreenivasan 1996). The three-dimensional box-counting algorithm is applied to the irrotational boundary. First, we divide the three-dimensional space into cubic boxes with size r_{box}, and then we count the minimum number of boxes $N(r_{box})$ needed to contain the whole irrotational boundary. The fractal dimension can be estimated with a power law $N \sim r_{box}^{-D_f}$, where D_f is the three-dimensional fractal dimension. Figure 16(a) plots $N/(L_x/\delta)$ against r_{box}/δ. The power law $N \sim r_{box}^{-D_f}$ is observed for a wide range of scales, suggesting that the irrotational boundary is characterized by a fractal shape. Even though the results are similar for all Re_θ, there are small variations with the increase of Re_θ. The fractal dimension D_f estimated from $N(r_{box})$ with range $15\eta_{TI} < r_{box} < 0.5\delta$ is plotted in figure 16(b). As the Reynolds number increases, D_f also increases. These values of the fractal dimension are slightly smaller than $D_f \approx 7/3$ found in previous studies (de Silva *et al.* 2013; Zhuang *et al.* 2018) for Reynolds numbers higher than in the present DNS, namely $Re_\theta \gg 13\,000$. However, Wu *et al.* (2020) have reported $D_f \approx 2.2$ at a low Reynolds number ($Re_\tau = 483$), and Borrell & Jiménez (2016) also showed that the fractal dimension is approximately 2.1–2.2 for $Re_\tau = 1000$–2000. Although D_f tends to increase with Re_θ, D_f is not expected to increase monotonically up to an infinite value with the Reynolds number. The increasing trend of D_f is possibly limited for small to moderately large Reynolds numbers.

The previous study (Meneveau & Sreenivasan 1990) suggested that the surface area can be estimated based on the fractal dimension assumption $A \sim L^2(\eta/L)^{2-D_f}$. This can be applied in the area of the irrotational boundary in TBLs as $A_{IB} \sim \delta^2(\eta_{TI}/\delta)^{2-D_f}$. Here, L can be replaced by δ, which represents the large-scale length in TBLs. The scaling law $A_{IB} \sim \delta^2(\eta_{TI}/\delta)^{2-D_f}$ is also examined by plotting $\delta^2(\eta_{TI}/\delta)^{2-D_f}/(A_{IB}\delta^2/(L_xL_z))$ against Re_θ in figure 17. The three-dimensional fractal dimension D_f used here is obtained

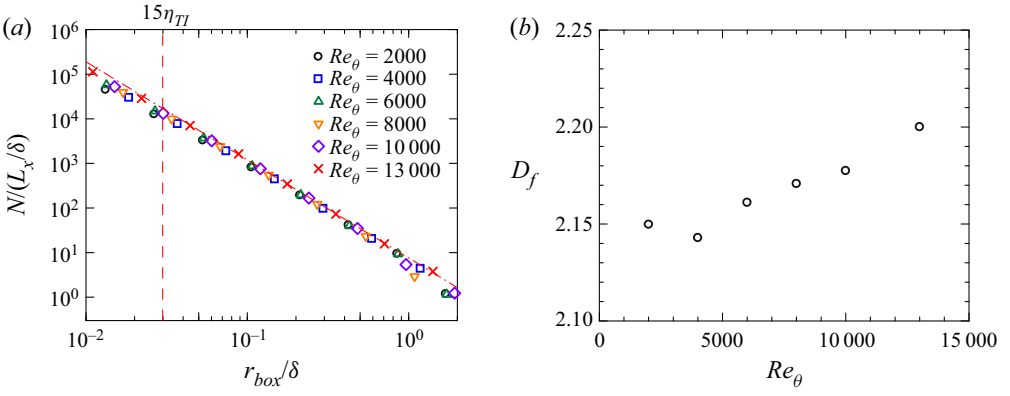

Figure 16. (*a*) Plots of $N/(L_x/\delta)$ against r_{box}/δ, where r_{box} is a box size, and N is the minimum number of boxes with size r_{box} for covering the whole irrotational boundary. The red dashed line denotes $15\eta_{TI}$ for $Re_\theta = 13\,000$. (*b*) The Reynolds number dependence of the values of three-dimensional box-counting fractal dimension D_f.

from the three-dimensional box-counting method shown above, and $A_{IB}\delta^2/(L_xL_z)$ represents the surface area of the irrotational boundary per δ^2. From the figure, $\delta^2(\eta_{TI}/\delta)^{2-D_f}/(A_{IB}\delta^2/(L_xL_z))$ is approximately 1 and independent of the Reynolds number; the surface area of the irrotational boundary also follows the fractal argument of the interface. This result also indicates that the D_f value obtained from figure 16(*a*) expresses accurately the fractal dimension of the irrotational boundary even though it is smaller than the 7/3 suggested in Sreenivasan, Ramshankar & Meneveau (1989) for turbulent flows (TBL, jet, mixing layer, etc.). These results also indicate that the boundary layer thickness and the Kolmogorov scale taken near the TNTI layer ($y_I/\delta_{TNTI} = -2$) are the largest and smallest length scales relevant to the geometry of the irrotational boundary.

3.6. *The entrainment process*

The entrainment is often explained by the combination of the local transition from non-turbulent to turbulent fluid near the TNTI and the non-turbulent fluid motions drawn directly towards the turbulent region, which are often called nibbling and engulfment, respectively (da Silva *et al.* 2014). Nibbling is also called local entrainment, which is represented as the propagation of irrotational boundary. Engulfment is caused by the large-scale motions in the flow, which draws directly the non-turbulent fluids towards the turbulent region without gain of vorticity. Previous studies (da Silva *et al.* 2014) also show that the growth of turbulence is caused mainly by the local entrainment in most types of flow. In the present study, we analyse the entrainment with a focus on nibbling.

The velocity of the irrotational boundary (enstrophy isosurface) movement $\boldsymbol{u}^I$ can be written as a sum of fluid velocity $\boldsymbol{u}$ and the propagation velocity $\boldsymbol{v}^P$, i.e. $\boldsymbol{u}^I = \boldsymbol{u} + \boldsymbol{v}^P$, where $\boldsymbol{v}^P = v_n\boldsymbol{n}$ is expressed with the local entrainment velocity v_n and the interface normal direction $\boldsymbol{n}$. By the propagation of the irrotational boundary to the non-turbulent region, non-turbulent fluids pass through the irrotational boundary to the turbulent region, and this local entrainment velocity can be derived with the enstrophy transport equation (Holzner & Lüthi 2011)

$$v_n = \frac{\mathrm{D}(\omega^2/2)/\mathrm{D}t}{|\nabla(\omega^2/2)|}. \tag{3.4}$$

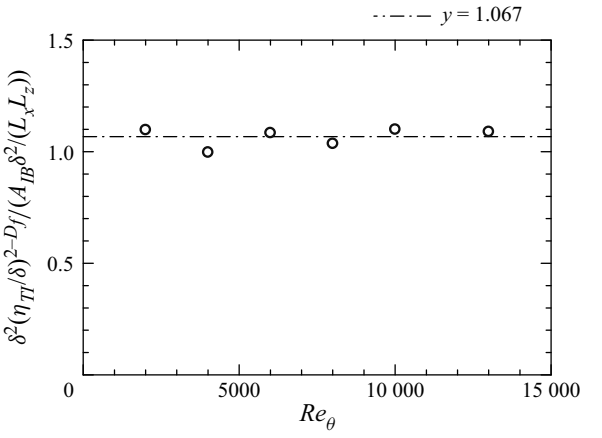

Figure 17. The scaling of the surface area of the irrotational boundary A_{IB}: $\delta^2(\eta_{TI}/\delta)^{2-D_f}/(A_{IB}\delta^2/(L_xL_z))$.

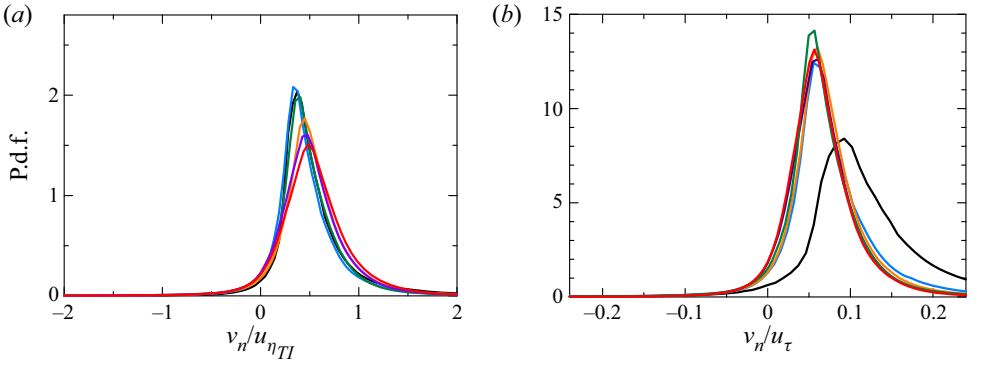

Figure 18. The p.d.f.s of the local entrainment velocity v_n normalized by (*a*) Kolmogorov velocity length scale $u_{\eta_{TI}}$, and (*b*) friction velocity u_τ. The line colours represent the Reynolds numbers as shown in figure 3.

The p.d.f.s of the local entrainment velocity v_n normalized by the Kolmogorov velocity $u_{\eta_{TI}} = (\langle\varepsilon\rangle_I\nu)^{1/4}$ and friction velocity u_τ are shown in figures 18(*a*) and 18(*b*), respectively. Here, the positive value of v_n indicates that the irrotational boundary propagates into the non-turbulent region, and vice versa. Large probability appears for $v_n > 0$, indicating that the irrotational boundary frequently propagates towards the non-turbulent region, which is similar to that found in Jahanbakhshi (2021) in the spatial TBL ($Re_\tau \approx 500$). For the p.d.f.s of v_n normalized by $u_{\eta_{TI}}$, their shapes and peaks differ depending on the Reynolds number. However, when v_n is normalized by the friction velocity u_τ, the p.d.f.s for $Re_\theta \geq 4000$ have a very similar shape although the profile is different for $Re_\theta = 2000$. The local entrainment process is often considered to be caused by the intense vorticity structures (worms) near the TNTI (da Silva *et al.* 2014). The intense vorticity structures are found to have radius approximately 4η and length approximately $3l$ (where l is the integral length scale) in HIT with Reynolds number range $Re_\lambda = 35$–170 (Jiménez *et al.* 1993). For the present DNS, $3l_{TI}$ satisfies $3l_{TI} \lesssim \delta$ according to the $Re_{\lambda.TI}$ in table 3 and η_{TI}/δ in figure 13(*a*). Furthermore, Marusic, Mathis & Hutchins (2010) showed that the small-scale component of u^2 with streamwise length $l_x < \delta$ in the outer layer is also Reynolds-number-independent for moderate and high Reynolds numbers if it

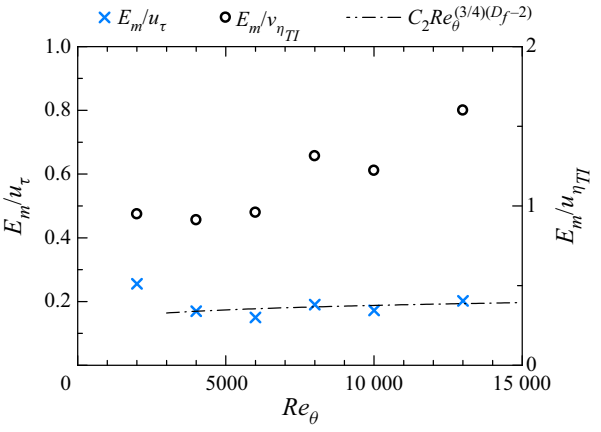

Figure 19. Normalized mean mass entrainment rate per unit horizontal area.

is normalized by the wall unit. In summary, the friction velocity is a reasonable velocity scale that characterizes the local entrainment velocity as long as the Reynolds number is not too small. Although the thickness of the TNTI layer scales with the Kolmogorov length scale, the local entrainment velocity is not well characterized by the Kolmogorov velocity scales. Previous studies on vortical structures within the TNTI layer have found that the characteristics of the TNTI layer are explained reasonably by the flow around small-scale vortex tubes (Watanabe *et al.* 2017*a*). As also observed for the TNTI layers in this study, the length and velocity of vortex tubes have different scalings: the vortex diameter scales with the Kolmogorov length scale while the velocity around vortices does not scale with the Kolmogorov velocity (Kang, Tanahashi & Miyauchi 2007; Mouri, Hori & Kawashima 2007; da Silva *et al.* 2011). These scalings of the vortices may appear as different scalings of the length and velocity scales of the TNTI layer.

The mean mass entrainment rate E_m per unit horizontal area is calculated as $E_m \approx \langle v_n \rangle A_{IB}/L_x L_y$, where the density is a constant due to the incompressibility. Figure 19 shows $E_m/u_{\eta_{TI}}$ and E_m/u_τ as functions of Re_θ. The fractal analysis has suggested that $\delta^2(\eta_{TI}/\delta)^{2-D_f}/(A_{IB}\delta^2/(L_x L_y)) \approx 1$, which yields $A_{IB}/(L_x L_y) \approx (\eta_{TI}/\delta)^{2-D_f}$. In addition, the scaling law for isotropic turbulence $\eta_{TI}/\delta \sim Re_\theta^{-3/4}$ can be used to obtain $A_{IB}/L_x L_y \approx Re^{(3/4)(D_f-2)}$. Also, the p.d.f. of v_n has suggested that $\langle v_n \rangle$ scales with u_τ. These relations yield the scaling law for the mean entrainment rate as $E_m/u_\tau \sim Re^{(3/4)(D_f-2)}$, which is also compared with the DNS results in figure 19 as the dot-dash line. Here, $D_f = 2.15$, which is an average of all Reynolds numbers, is used. In the present DNS, the mean entrainment rate E_m normalized by u_τ tends to follow this scaling law for $Re_\theta \geq 4000$. The departure from the scaling law for $Re_\theta = 2000$ is explained by two points: the turbulence under the TNTI becomes far from an isotropic state at low Re_θ, as in the results for η_{TI}/δ in figure 13(*a*); the entrainment velocity $\langle v_n \rangle/u_\tau$ at $Re_\theta = 2000$ has a different profile from higher Reynolds numbers, as shown in figure 18(*b*). These can be explained in the following physical view: y/δ_v or $y+$ corresponding to the intermittent region is very small for a low Reynolds number. Therefore, the small-scale turbulent motions in the intermittent region are affected strongly by the viscous effects from the wall, which result in a large viscous dissipation ratio for turbulent kinetic energy ε_{TI}, namely, a small Kolmogorov length scale η_{TI}. Similarly, the enhanced viscous effects near the TNTI result in a large local entrainment velocity, which is dominated by the

viscous effects on vorticity. However, the direct wall effects on the small-scale motions in the intermittent region become weaker with the increase of the Reynolds number. On the other hand, the large-scale motions in the intermittent region also become prominent with the increase of the Reynolds number. Consequently, a larger proportion of small-scale motions is generated from the large-scale motions by the scale-by-scale interaction in the intermittent region at a higher Reynolds number. Therefore, the flow tends to be closer to isotropic turbulence at a higher Reynolds number.

4. Conclusion

We performed DNS of the temporally developing TBL with a wide range of Reynolds numbers Re_θ from 2000 to 13 000 to investigate the Reynolds number dependence of the TNTI layer. The grid spacing is determined so that the small-scale turbulent motions near the TNTI layer are well resolved. The outer edge of the TNTI layer (the irrotational boundary) detected as an isosurface of vorticity magnitude is smooth and looks similar to those in free shear flows. The mean thicknesses of the TNTI layer (δ_{TNTI}), TSL (δ_{TSL}) and VSL (δ_{VSL}) defined with the gradient of the conditional mean vorticity magnitude and vorticity dynamics are approximately 15, 10 and 5 times Kolmogorov scale η_{TI}, where η_{TI} is taken from the turbulent region near the TNTI layer. On the other hand, δ_{TNTI}, δ_{TSL} and δ_{VSL} normalized by the Taylor microscale decrease with the Reynolds number. The profiles of the conditional mean vorticity and the second invariant of the velocity gradient tensor at different Re_θ also collapse well when they are normalized by statistics taken near the TNTI layer and the distance from the irrotational boundary is normalized by η_{TI}.

The conditional mean streamwise velocity $\langle u\rangle_I$ is almost constant within the VSL, while $\langle u\rangle_I$ increases rapidly towards the turbulent core region existing within the TSL. The mean velocity jump across the TSL is the order of the r.m.s. streamwise velocity fluctuation near the TNTI layer. The effects of the mean shear near the TNTI layer are evaluated with the conditional shear parameter S_I^*, defined as the time scale ratio of the large-scale turbulent motions to the mean shear, and the shear-to-vorticity ratio S_I/ω_I'. S_I^* is approximately 4 near the TNTI layer for all Reynolds numbers, indicating that the mean shear effects are not significant on large-scale eddies. Here, S_I/ω_I' is approximately 0.1–0.2 and decreases with the Reynolds number, which implies that the shear effects on the small-scale turbulent motions are weak and tend to be isotropic with the increase of the Reynolds number. The ratio between the smallest and largest scales of turbulent motion near the TNTI layer exhibits the relation $\eta_{TI}/\delta \sim Re_\theta^{-3/4}$, except for the low Reynolds number case. Higher isotropy near the TNTI at a larger Reynolds number has also been confirmed with the second invariants of anisotropy tensors of Reynolds stress and vorticity.

The geometry of the irrotational boundary was also studied in terms of the mean curvature and the surface area. A peak in the p.d.f. of the mean curvature normalized by η_{TI} hardly changes with the Reynolds number, where most of the irrotational boundary has curvature radius approximately $40\eta_{TI}$, which is the typical length scale of velocity gradients in the outer logarithmic layer and outer layer (Jiménez 2013). With flow visualization, previous studies observed small-scale vortex tubes within the TNTI layer, and the interface forms around them. The curvature of the TNTI is expected to be related to the diameter of the vortices or the curvature radius of the vortex axis since both the curvature radius of the TNTI and the length scale of vortex tubes scale with the Kolmogorov scale. The surface area of the irrotational boundary increases with the Reynolds number, where the Reynolds number dependence is consistent with the fractal

analysis of the interface. The fractal dimension is measured as 2.14–2.20 and increases slowly with the Reynolds number.

The entrainment process related to nibbling is investigated with the local entrainment velocity and the mean entrainment rate. The p.d.f. of local entrainment velocity v_n shows that the friction velocity u_τ is a reasonable velocity scale that characterizes the local entrainment velocity v_n. The mean entrainment rate per unit horizontal area E_m normalized by u_τ follows the scaling law $E_m/u_\tau \sim Re^{3/4(D_f-2)}$ for $Re_\theta \geq 4000$.

Acknowledgements. The authors acknowledge Professor J. Jiménez and Professor C. Pan for providing valuable comments. The direct numerical simulations presented in this manuscript were carried out on the high-performance computing system in the Japan Agency for Marine-Earth Science and Technology.

Funding. This work was partially supported by Collaborative Research Project on Computer Science with High-Performance Computing in Nagoya University, JSPS KAKENHI grant nos 20H05754, 22K03903 and 22H01398, and National Natural Science Foundation of China grant no. 91852206.

Declaration of interests. The authors report no conflict of interest.

Author ORCIDs.
Xinxian Zhang https://orcid.org/0000-0002-6010-5352;
Tomoaki Watanabe https://orcid.org/0000-0002-9375-0075;
Koji Nagata https://orcid.org/0000-0002-8519-5454.

Appendix A. Numerical methods

The numerical code used in the present DNS is based on the fractional step method with staggered grids as used in Watanabe *et al.* (2018*b*). The fully conservative central difference schemes (Morinishi *et al.* 1998) are applied for spatial discretization, where the accuracy is fourth order in the x and z directions, and second order in the y direction. The third-order Runge–Kutta method is used for temporal advancement, while the biconjugate gradient stabilized (Bi-CGSTAB) method (Van der Vorst 1992) is used to solve the Poisson equation for pressure.

An early time period of the flow is simulated by using an implicit large eddy simulation (ILES) like the one conducted in our previous study (Tanaka, Watanabe & Nagata 2019), where the effects of subgrid scales are modelled implicitly by a tenth-order low-pass filter presented in Kennedy & Carpenter (1994), while other numerical schemes are the same as in the DNS. After the TBL fully develops in the ILES, the ILES results are used to initialize the DNS. Here, the ILES is assumed to resolve most length scales of the flow (at least scales greater than 20 times Kolmogorov scale) to fully recover the small-scale velocity fluctuations in the DNS (Lalescu, Meneveau & Eyink 2013). The number of the grid points used in the ILES ($N_{xLES}, N_{yLES}, N_{zLES}$) for different Reynolds numbers is summarized in table 4, which gives the grid sizes $\Delta_x \leq 12\eta$, $\Delta_y \leq 3\eta$ and $\Delta_y \leq 6\eta$ during the simulation. Therefore, most length scales of turbulence in the TBL are resolved in the ILES. After the DNS are switched from the ILES, time is advanced longer than the integral time scale. It was confirmed that the present DNS at the end of the simulations reproduces well-known small-scale characteristics of turbulence, and the details can be found in our previous study (Watanabe *et al.* 2019*b*).

Case	Re_θ	N_{xLES}	N_{yLES}	N_{zLES}
B02	2000	288	300	288
B04	4000	648	648	648
B06	6000	864	864	864
B08	8000	1152	1152	1152
B10	10 000	1458	1458	1458
B13	13 000	1728	1944	1728

Table 4. The number of grid points for LES used to initialize the DNS of the temporally developing TBL.

Appendix B. The effects of the computational domain size on the TNTI characteristics

This appendix examines the effects of the finite computational domain size on the characteristics of the TNTI layer because the large-scale structures in the streamwise direction develop in the TBL. We have conducted additional DNS with a large computational size in the streamwise direction $L_x = 13.4\delta$ at $Re_\theta = 2000$ (case LB02). The initial conditions and numerical methods are the same as for the other simulations in the present study. The computational parameters are displayed in table 5, where δ is taken at the end of the simulation. Although the length of large-scale motions increases with the Reynolds number, their length normalized by δ hardly increases with the Reynolds number as investigated in previous studies (Lozano-Durán & Jiménez 2014; Sillero, Jiménez & Moser 2014; Lee *et al.* 2017). Therefore, the comparison between B02 and LB02 is still useful to assess the domain size effects on the TNTI for large-scale motions at higher Reynolds numbers.

The statistics of the TNTI layer are compared between B02 and LB02. For both cases, the same threshold $\hat{\omega}_{th} = 10^{2.5}$ is used to detect the irrotational boundary. The conditional profiles of mean vorticity $\langle\omega\rangle_I$ and its derivative $\langle\omega\rangle_I' = -\mathrm{d}\langle\omega\rangle_I/\mathrm{d}y_I$ with y_I are compared in figure 20(a), which is used to determine the mean thickness of the TNTI layer. The difference between the two cases is very small and is expected to be caused by a different level of statistical convergence because more samples are available in LB02. The conditional profiles of Kolmogorov length scale η_I are shown in figure 20(b), where y_I is normalized by the mean thickness of the TNTI layer, δ_{TNTI}. The conditional profile of η_I hardly differs between B02 and LB02. These results indicate that the conditional statistics of small-scale quantities hardly depend on the domain size larger than $2\pi\delta$, which is used in B02.

The domain size effect should also be examined for large-scale characteristics of the TNTI layer. The large-scale properties of the TNTI layer assessed in the present work are fractal dimension D and surface area A_{IB}, which are examined by comparing B02 and LB02 in figure 21. Here, figure 21(a) shows the number of boxes needed to cover the irrotational boundary. The results for B02 and LB02 are almost identical, and the fractal dimension is evaluated accurately in B02. Figure 21(b) compares the surface area A_{IB} between LB02 and other DNS. The figure also includes DNS results of spatially developing TBL by Borrell *et al.* (2013). The surface area is also hardly influenced by the domain size. The present DNS results also agree with the spatial TBLs, which are simulated with a large domain size in the streamwise direction. Therefore, the large-scale properties of the TNTI layer in the present study are well resolved within the DNS with $Lx \approx 2\pi\delta$.

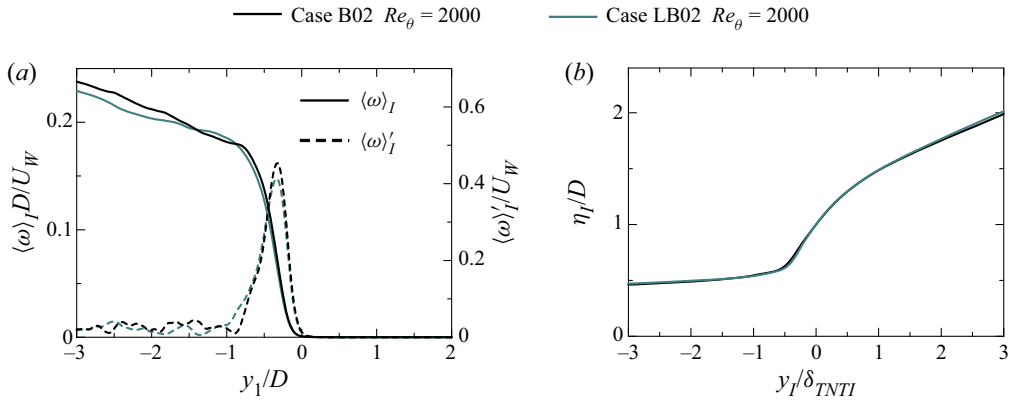

Figure 20. (*a*) Conditional mean vorticity and its derivative with respect to y_I. (*b*) Conditional profiles of Kolmogorov length scale η_I. The different colours of the lines represent cases B02 and LB02.

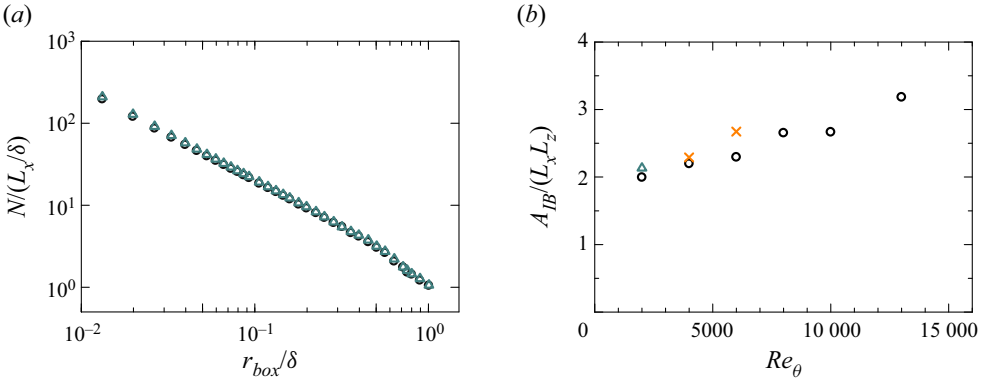

Figure 21. The domain size effects on the fractal analysis and the surface area of the irrotational boundary. (*a*) Plot of $N/(L_x/\delta)$ against r_{box}/δ, where r_{box} is a box size and N is the minimum number of boxes with size r_{box} for covering the whole irrotational boundary. (*b*) The surface area of irrotational boundary A_{IB} plotted against Re_θ. The green triangles represent the results of LB02 ($L_x = 13.4\delta$), while the orange crosses represent the DNS results of spatial TBLs in Borrell, Sillero & Jiménez (2013).

Case	Re_θ	N_x	N_y	N_z	L_x/D	L_y/D	L_z/D	L_x/δ	L_y/δ	L_z/δ
LB02	2000	2048	648	512	112	76	28	13.4	9.1	3.4

Table 5. Computational parameters and computational domain size at the end of the simulation for case LB02.

The influence of the domain size in the direction for which periodicity is assumed has also been discussed in previous studies for channel flow (Lozano-Durán & Jiménez 2014; Abe, Antonia & Toh 2018). Their results show that the computational domain with $L_x = 2\pi h$ is large enough to reproduce the one-point statistics of DNS with $L_x = 4\pi h$ or $L_x = 8\pi h$, where h is the half-width of the channel. Also, Lozano-Durán & Jiménez (2014) observed that the one-dimensional energy spectra in the streamwise direction computed from the medium domain ($L_x = 2\pi h$) agree with those from the larger domain ($L_x = 4\pi h$)

until they are truncated at the maximum wavelengths fitting in the domain. This has also been confirmed with the two-dimensional spectrum (Lozano-Durán & Jiménez 2014), which has been compared between $L_x = 4\pi h$ and $L_x = 8\pi h$. del Álamo *et al.* (2004) also observed that the resolved part of the velocity spectrum is not strongly affected by the size of the domain. Lozano-Durán & Jiménez (2014) found that even the identified uv structures with length close to the box size ($l_x > 3h$, $L_x = 2\pi h$) are strongly affected by the box size, which is caused by the accumulation of structures that are longer than the box size L_x, but the uv structures with smaller length are not affected by the domain size. Based on these observations, Lozano-Durán & Jiménez (2014) argued that even though the large structures with $l_x > L_x$ are essentially infinitely long in a small computational domain with $L_x \approx 2\pi h$ with the periodic boundary conditions, their interaction with the well-resolved scales is represented correctly. This argument was also confirmed by a comparison of two-point correlations between different domain sizes in channel flow, which was also found to be Reynolds-number-independent (Sillero *et al.* 2014). These results are also related to the negligible influences of the domain size on the characteristics of the TNTI layer.

In conclusion, the small-scale motions and large-scale properties related to the TNTI in the present work are all well replicated in our present DNS with domain size $L_x = 2\pi\delta$.

References

Abe, H., Antonia, R.A. & Toh, S. 2018 Large-scale structures in a turbulent channel flow with a minimal streamwise flow unit. *J. Fluid Mech.* **850**, 733–768.

Adrian, R.J., Meinhart, C.D. & Tomkins, C.D. 2000 Vortex organization in the outer region of the turbulent boundary layer. *J. Fluid Mech.* **422**, 1–54.

del Álamo, J.C., Jiménez, J., Zandonade, P. & Moser, R.D. 2004 Scaling of the energy spectra of turbulent channels. *J. Fluid Mech.* **500**, 135–144.

Attili, A., Cristancho, J.C. & Bisetti, F. 2014 Statistics of the turbulent/non-turbulent interface in a spatially developing mixing layer. *J. Turbul.* **15** (9), 555–568.

Bisset, D.K., Hunt, J.C.R. & Rogers, M.M. 2002 The turbulent/non-turbulent interface bounding a far wake. *J. Fluid Mech.* **451**, 383–410.

Borrell, G. & Jiménez, J. 2016 Properties of the turbulent/non-turbulent interface in boundary layers. *J. Fluid Mech.* **801**, 554–596.

Borrell, G., Sillero, J.A. & Jiménez, J. 2013 A code for direct numerical simulation of turbulent boundary layers at high Reynolds numbers in BG/P supercomputers. *Comput. Fluids* **80**, 37–43.

Carlier, J. & Stanislas, M. 2005 Experimental study of eddy structures in a turbulent boundary layer using particle image velocimetry. *J. Fluid Mech.* **535**, 143–188.

Chauhan, K., Philip, J., de Silva, C.M., Hutchins, N. & Marusic, I. 2014*b* The turbulent/non-turbulent interface and entrainment in a boundary layer. *J. Fluid Mech.* **742**, 119–151.

Chauhan, K., Philip, J. & Marusic, I. 2014*a* Scaling of the turbulent/non-turbulent interface in boundary layers. *J. Fluid Mech.* **751**, 298–328.

Cimarelli, A. & Boga, G. 2021 Numerical experiments on turbulent entrainment and mixing of scalars. *J. Fluid Mech.* **927**, A34.

Corrsin, S. 1958 Local isotropy in turbulent shear flow. *NACA Tech. Rep.* 58B11.

Corrsin, S. & Kistler, A.L. 1955 Free-stream boundaries of turbulent flows. *NACA Tech. Rep.* 1244.

Crow, S. 1968 Turbulent Rayleigh shear flow. *J. Fluid Mech.* **32**, 113–130.

De Graaff, D.B. & Eaton, J.K. 2000 Reynolds-number scaling of the flat-plate turbulent boundary layer. *J. Fluid Mech.* **422**, 319–346.

Eisma, J., Westerweel, J., Ooms, G. & Elsinga, G.E. 2015 Interfaces and internal layers in a turbulent boundary layer. *Phys. Fluids* **27** (5), 055103.

Erm, L.P. & Joubert, P.N. 1991 Low-Reynolds-number turbulent boundary layers. *J. Fluid Mech.* **230**, 1–44.

Guarini, S.E., Moser, R.D., Shariff, K. & Wray, A. 2000 Direct numerical simulation of a supersonic turbulent boundary layer at Mach 2.5. *J. Fluid Mech.* **414**, 1–33.

HAWKES, E.R., SANKARAN, R., SUTHERLAND, J.C. & CHEN, J.H. 2007 Scalar mixing in direct numerical simulations of temporally evolving plane jet flames with skeletal CO/H_2 kinetics. *Proc. Combust. Inst.* **31**, 1633–1640.

HOLZNER, M. & LÜTHI, B. 2011 Laminar superlayer at the turbulence boundary. *Phys. Rev. Lett.* **106** (13), 134503.

HOLZNER, M., LIBERZON, A., NIKITIN, N., KINZELBACH, W. & TSINOBER, A. 2007 Small-scale aspects of flows in proximity of the turbulent/nonturbulent interface. *Phys. Fluids* **19** (7), 071702.

HUNT, J.C.R., EAMES, I., WESTERWEEL, J., DAVIDSON, P.A., VOROPAYEV, S., FERNANDO, J. & BRAZA, M. 2010 Thin shear layers – the key to turbulence structure? *J. Hydro-Environ. Res.* **4** (2), 75–82.

ISHIHARA, T., OGASAWARA, H. & HUNT, J.C.R. 2015 Analysis of conditional statistics obtained near the turbulent/non-turbulent interface of turbulent boundary layers. *J. Fluids Struct.* **53**, 50–57.

JAHANBAKHSHI, R. 2021 Mechanisms of entrainment in a turbulent boundary layer. *Phys. Fluids* **33** (3), 035105.

JAHANBAKHSHI, R., VAGHEFI, N.S. & MADNIA, C.K. 2015 Baroclinic vorticity generation near the turbulent/non-turbulent interface in a compressible shear layer. *Phys. Fluids* **27** (10), 105105.

JIMÉNEZ, J. 2013 Near-wall turbulence. *Phys. Fluids* **25** (10), 101302.

JIMÉNEZ, J., WRAY, A.A., SAFFMAN, P.G. & ROGALLO, R.S. 1993 The structure of intense vorticity in isotropic turbulence. *J. Fluid Mech.* **255**, 65–90.

KANG, S.J., TANAHASHI, M. & MIYAUCHI, T. 2007 Dynamics of fine scale eddy clusters in turbulent channel flows. *J. Turbul.* **8**, N52.

KENNEDY, C.A. & CARPENTER, M.H. 1994 Several new numerical methods for compressible shear-layer simulations. *Appl. Numer. Maths* **14** (4), 397–433.

KOZUL, M., CHUNG, D. & MONTY, J.P. 2016 Direct numerical simulation of the incompressible temporally developing turbulent boundary layer. *J. Fluid Mech.* **796**, 437–472.

LALESCU, C.C., MENEVEAU, C. & EYINK, G.L. 2013 Synchronization of chaos in fully developed turbulence. *Phys. Rev. Lett.* **110** (8), 084102.

LEE, J., SUNG, H.J. & ZAKI, T.A. 2017 Signature of large-scale motions on turbulent/non-turbulent interface in boundary layers. *J. Fluid Mech.* **819**, 165–187.

LONG, Y., WANG, J. & PAN, C. 2022 Universal modulations of large-scale motions on entrainment of turbulent boundary layers. *J. Fluid Mech.* **941**, A68.

LOZANO-DURÁN, A. & JIMÉNEZ, J. 2014 Effect of the computational domain on direct simulations of turbulent channels up to $Re_\tau = 4200$. *Phys. Fluids* **26** (1), 011702.

MARTÍN, M.P. 2007 Direct numerical simulation of hypersonic turbulent boundary layers. Part 1. Initialization and comparison with experiments. *J. Fluid Mech.* **570**, 347.

MARUSIC, I., MATHIS, R. & HUTCHINS, N. 2010 High Reynolds number effects in wall turbulence. *Intl J. Heat Fluid Flow* **31** (3), 418–428.

MARUSIC, I., MONTY, J.P., HULTMARK, M. & SMITS, A.J 2013 On the logarithmic region in wall turbulence. *J. Fluid Mech.* **716**, R3.

MENEVEAU, C. & SREENIVASAN, K.R. 1990 Interface dimension in intermittent turbulence. *Phys. Rev.* A **41** (4), 2246.

MISTRY, D., PHILIP, J., DAWSON, J.R. & MARUSIC, I. 2016 Entrainment at multi-scales across the turbulent/non-turbulent interface in an axisymmetric jet. *J. Fluid Mech.* **820**, 690–725.

MORINISHI, Y., LUND, T.S., VASILYEV, O.V. & MOIN, P. 1998 Fully conservative higher order finite difference schemes for incompressible flow. *J. Comput. Phys.* **143** (1), 90–124.

MOSER, R.D., KIM, J. & MANSOUR, N.N. 1999 Direct numerical simulation of turbulent channel flow up to $Re_\tau = 590$. *Phys. Fluids* **11** (4), 943–945.

MOURI, H., HORI, A. & KAWASHIMA, Y. 2007 Laboratory experiments for intense vortical structures in turbulence velocity fields. *Phys. Fluids* **19** (5), 055101.

NAGATA, R., WATANABE, T. & NAGATA, K. 2018 Turbulent/non-turbulent interfaces in temporally evolving compressible planar jets. *Phys. Fluids* **30** (10), 105109.

NEAMTU-HALIC, M.M., KRUG, D., MOLLICONE, J.P., VAN REEUWIJK, M., HALLER, G. & HOLZNER, M. 2020 Connecting the time evolution of the turbulence interface to coherent structures. *J. Fluid Mech.* **898**, A30.

OSAKA, H., KAMEDA, T. & MOCHIZUKI, S. 1998 Re-examination of the Reynolds-number-effect on the mean flow quantities in a smooth wall turbulent boundary layer. *JSME Intl J.* B **41** (1), 123–129.

PHILIP, J., MENEVEAU, C., DE SILVA, C.M. & MARUSIC, I. 2014 Multiscale analysis of fluxes at the turbulent/non-turbulent interface in high Reynolds number boundary layers. *Phys. Fluids* **26** (1), 015105.

POPE, S.B. 2000 *Turbulent Flows*. Cambridge University Press.

PRANDTL, L. 1928 Motion of fluids with very little viscosity. *Tech. Memo. Natn. Advis. Comm. Aeronaut. Wash.* No. 452, pp. 484–491.

PRASAD, R.R. & SREENIVASAN, K.R. 1996 Scalar interfaces in digital images of turbulent flows. *Exp. Fluids* **7**, 259–264.

VAN REEUWIJK, M. & HOLZNER, M. 2014 The turbulence boundary of a temporal jet. *J. Fluid Mech.* **739**, 254–275.

VAN REEUWIJK, M., VASSILICOS, J.C. & CRASKE, J. 2021 Unified description of turbulent entrainment. *J. Fluid Mech.* **908**, A12.

SCHLATTER, P. & ÖRLÜ, R. 2010 Assessment of direct numerical simulation data of turbulent boundary layers. *J. Fluid Mech.* **659**, 116–126.

SCHLATTER, P. & ÖRLÜ, R. 2012 Turbulent boundary layers at moderate Reynolds numbers: inflow length and tripping effects. *J. Fluid Mech.* **710**, 5–34.

SILLERO, J.A., JIMÉNEZ, J. & MOSER, R.D. 2013 One-point statistics for turbulent wall-bounded flows at Reynolds numbers up to $\delta^+ \approx 2000$. *Phys. Fluids* **25** (10), 105102.

SILLERO, J.A., JIMÉNEZ, J. & MOSER, R.D. 2014 Two-point statistics for turbulent boundary layers and channels at Reynolds numbers up to $\delta^+ \approx 2000$. *Phys. Fluids* **26** (10), 105109.

DA SILVA, C.B., DOS REIS, R.J.N. & PEREIRA, J.C.F. 2011 The intense vorticity structures near the turbulent/non-turbulent interface in a jet. *J. Fluid Mech.* **685**, 165–190.

DA SILVA, C.B., HUNT, J.C.R., EAMES, I. & WESTERWEEL, J. 2014 Interfacial layers between regions of different turbulence intensity. *Annu. Rev. Fluid Mech.* **46**, 567–590.

DA SILVA, C.B. & PEREIRA, J.C.F. 2008 Invariants of the velocity-gradient, rate-of-strain, and rate-of-rotation tensors across the turbulent/nonturbulent interface in jets. *Phys. Fluids* **20** (5), 055101.

DE SILVA, C.M., PHILIP, J., CHAUHAN, K., MENEVEAU, C. & MARUSIC, I. 2013 Multiscale geometry and scaling of the turbulent-nonturbulent interface in high Reynolds number boundary layers. *Phys. Rev. Lett.* **111** (4), 044501.

DE SILVA, C.M., PHILIP, J., HUTCHINS, N. & MARUSIC, I. 2017 Interfaces of uniform momentum zones in turbulent boundary layers. *J. Fluid Mech.* **820**, 451–478.

SILVA, T.S., ZECCHETTO, M. & DA SILVA, C.B. 2018 The scaling of the turbulent/non-turbulent interface at high Reynolds numbers. *J. Fluid Mech.* **843**, 156–179.

SMITS, A.J., MCKEON, B.J. & MARUSIC, I. 2011 High-Reynolds number wall turbulence. *Annu. Rev. Fluid Mech.* **43**, 353–375.

SPALART, P.R 1988 Direct simulation of a turbulent boundary layer up to $R_\theta = 1410$. *J. Fluid Mech.* **187**, 61–98.

SREENIVASAN, K.R., RAMSHANKAR, R. & MENEVEAU, C.H. 1989 Mixing, entrainment and fractal dimensions of surfaces in turbulent flows. *Proc. R. Soc. Lond.* A **421**, 79–108.

TANAKA, S., WATANABE, T. & NAGATA, K. 2019 Multi-particle model of coarse-grained scalar dissipation rate with volumetric tensor in turbulence. *J. Comput. Phys.* **389**, 128–146.

TAVEIRA, R.R. & DA SILVA, C.B. 2014 Characteristics of the viscous superlayer in shear free turbulence and in planar turbulent jets. *Phys. Fluids* **26** (2), 021702.

TAVEIRA, R.R., DIOGO, J.S., LOPES, D.C. & DA SILVA, C.B. 2013 Lagrangian statistics across the turbulent–nonturbulent interface in a turbulent plane jet. *Phys. Rev.* E **88** (4), 043001.

VAN DER VORST, H.A. 1992 Bi-CGSTAB: a fast and smoothly converging variant of Bi-CG for the solution of nonsymmetric linear systems. *SIAM J. Sci. Stat. Comput.* **13** (2), 631–644.

VREMAN, A.W., SANDHAM, N.D. & LUO, K.H. 1996 Compressible mixing layer growth rate and turbulence characteristics. *J. Fluid Mech.* **320**, 235–258.

WATANABE, T., DA SILVA, C.B. & NAGATA, K. 2019*a* Non-dimensional energy dissipation rate near the turbulent/non-turbulent interfacial layer in free shear flows and shear free turbulence. *J. Fluid Mech.* **875**, 321–344.

WATANABE, T., DA SILVA, C.B., NAGATA, K. & SAKAI, Y. 2017*c* Geometrical aspects of turbulent/non-turbulent interfaces with and without mean shear. *Phys. Fluids* **29** (8), 085105.

WATANABE, T., JAULINO, R., TAVEIRA, R.R., DA SILVA, C.B., NAGATA, K. & SAKAI, Y. 2017*a* Role of an isolated eddy near the turbulent/non-turbulent interface layer. *Phys. Rev. Fluids* **2** (9), 094607.

WATANABE, T., RILEY, J.J. & NAGATA, K. 2017*b* Turbulent entrainment across turbulent–nonturbulent interfaces in stably stratified mixing layers. *Phys. Rev. Fluids* **2** (10), 104803.

WATANABE, T., RILEY, J.J., NAGATA, K., ONISHI, R. & MATSUDA, K. 2018*a* A localized turbulent mixing layer in a uniformly stratified environment. *J. Fluid Mech.* **849**, 245–276.

WATANABE, T., SAKAI, Y., NAGATA, K., ITO, Y. & HAYASE, T. 2014 Wavelet analysis of coherent vorticity near the turbulent/non-turbulent interface in a turbulent planar jet. *Phys. Fluids* **26** (9), 095105.

WATANABE, T., SAKAI, Y., NAGATA, K., ITO, Y. & HAYASE, T. 2015 Turbulent mixing of passive scalar near turbulent and non-turbulent interface in mixing layers. *Phys. Fluids* **27** (8), 085109.

WATANABE, T., ZHANG, X. & NAGATA, K. 2018*b* Turbulent/non-turbulent interfaces detected in DNS of incompressible turbulent boundary layers. *Phys. Fluids* **30** (3), 035102.

WATANABE, T., ZHANG, X. & NAGATA, K. 2019*b* Direct numerical simulation of incompressible turbulent boundary layers and planar jets at high Reynolds numbers initialized with implicit large eddy simulation. *Comput. Fluids* **194**, 104314.

WESTERWEEL, J., FUKUSHIMA, C., PEDERSEN, J.M. & HUNT, J.C.R. 2009 Momentum and scalar transport at the turbulent/non-turbulent interface of a jet. *J. Fluid Mech.* **631**, 199–230.

WU, D., WANG, J., CUI, G. & PAN, C. 2020 Effects of surface shapes on properties of turbulent/non-turbulent interface in turbulent boundary layers. *Sci. China Technol. Sci.* **63** (2), 214–222.

ZHANG, X., WATANABE, T. & NAGATA, K. 2018 Turbulent/nonturbulent interfaces in high-resolution direct numerical simulation of temporally evolving compressible turbulent boundary layers. *Phys. Rev. Fluids* **3** (9), 094605.

ZHUANG, Y., TAN, H., HUANG, H., LIU, Y. & ZHANG, Y. 2018 Fractal characteristics of turbulent-non-turbulent interface in supersonic turbulent boundary layers. *J. Fluid Mech.* **843**, R2.